Universal Multifractals: Theory and Observations for Rain and Clouds

Y. TESSIER, S. LOVEJOY, AND D. SCHERTZER*

Department of Physics, McGill University, Montreal, Quebec, Canada

(Manuscript received 21 August1991, in final form 13 May 1992)

ABSTRACT

The standard model of atmospheric motions divides the atmosphere into distinct two- and three-dimensional isotropic turbulent regimes separated by a dimensional transition, the "mesoscale gap." It is argued that the "gap" is fictional and that the atmosphere is scaling but anisotropic at all scales. According to this alternative unified scaling model, the dynamics are governed by anisotropic (differentially stratified and rotating) cascade processes yielding highly variable multifractal fields. Just as Gaussian random variables are associated with (linear) sums of random variables, these (nonlinear) multiplicative processes are generically associated with (special) universal multifractals in which many of the details of the dynamics are irrelevant. Although an attempt is made to outline these arguments in a widely accessible form, they are not new to this paper; they provide its context and motivation. The principal purpose of this paper is to test these ideas empirically. This is done using Landsat, *NOAA-9,* and Meteosat cloud radiances at visible, near-infrared, and thermal infrared wavelengths with length scales spanning the range 166 m–4000 km, radar reflectivities of rain (in the horizontal, vertical, and time), and global daily rainfall accumulations. Spectral analysis, as well as the new double trace moment data-analysis technique, is applied. In each case, rather than the sharp dimensional transition predicted by the standard model, the scaling is found to be relatively well respected right through the mesoscale. The three fundamental universal multifractal exponents are then estimated and one can go on to outline how these exponents (with the help of appropriate space–time transformations) can be used to make dynamic multifractal models.

1. Introduction

a. The standard model in doubt and the alternative unified scaling model

The standard model of atmospheric dynamics (e.g., Monin 1972) divides the atmosphere into two fundamentally distinct regimes: a small-scale three-dimensional turbulent regime and a large-scale two-dimensional turbulent regime. Both regimes are scaling (scale invariant, power-law spectra) and both are considered self-similar (the combination of scaling with statistical isotropy). Unlike turbulence in three dimensions, in two dimensions, vortex stretching is inhibited and vorticity is conserved. This leads to qualitatively distinct two-dimensional and three-dimensional behavior: the standard model assumes that these different regimes are separated by a "mesoscale gap" whose scale is expected to be of the order of the scale height of the atmosphere (approximately 10 km).

The existence of the gap has been periodically questioned on empirical grounds since the late 1960s. However, we believe that an equally significant source of doubt concerns its theoretical underpinnings, which now appear to be quite ad hoc. This change in perception is possible due to the remarkable progress in scaling ideas that occurred during the 1980s. During that period, scaling ideas were extended beyond the restrictive bounds of the fractal geometry of sets to directly deal with the multifractal statistics (and dynamics) of fields. Multifractals are increasingly understood as providing the natural framework for scale-invariant nonlinear dynamics. Furthermore, due to the existence of stable attractive multifractal generators (Schertzer and Lovejoy 1987b, 1989a,b, 1991a; Schertzer et al. 1988; Fan 1989; Gupta and Waymire 1990; Brax and Peschanski 1991), they provide attractive physical models. This implies that many of the details of the dynamics are irrelevant and leads to new and powerful multifractal simulation and analysis techniques (some of which will be described below).

Scaling ideas have also been enriched by extensions in quite a different direction: scaling anisotropy. Recall that a scaling system is one in which small- and large-scale (statistical) properties are related by a scale-changing operation involving only the scale ratio: there

---

* Laboratoire de Météorologie Dynamique, Université Pierre et Marie Curie, Paris, France.

Corresponding author address: Y. Tessier, Laboratoire de Géologie Appliqueé, tour 15, 5ième étage, Boite 123, 4 Place Jussieu, 75252 Paris, Cedex 05, France.

is no characteristic size. Until recently, this scale change was restricted to ordinary "zooms" or magnifications. This is the isotropic self-similar scaling that provides the theoretical basis of the standard model referred to above. The only generalization of scaling beyond self-similarity was a slight variation called self-affinity, which combined the zoom with a (differential) "squashing" along certain fixed directions (e.g., coordinate axes). While this extension is in fact important in accounting for atmospheric stratification (associated with the existence of different spectral exponents in the horizontal and vertical directions) (Schertzer and Lovejoy 1983, 1985a,b), it is still very special. In particular, it was realized that geophysical applications generally involve not only differential stratification but also differential rotation (e.g., due to the Coriolis force). The need to extend scaling ideas to account for this observed geophysical anisotropy lead to the formalism of generalized scale invariance[1] (GSI, Schertzer and Lovejoy 1985b, 1987a,b, 1989a,b, 1991a; Lovejoy and Schertzer 1985). GSI goes beyond self-affinity: not only does it involve both differential rotation and stratification, but both effects can vary from place to place in either deterministic or even random manners. Indeed, GSI is such a general symmetry that the ad hoc nature of the standard picture (which arbitrarily postulates first isotropy and only then scaling) is quite obvious. It is far more natural to simply postulate scaling but without any a priori restrictions about isotropy.

b. *The role of satellite radiances and radar reflectivities*

Even before the theoretical basis of the standard model was brought into question, a series of in situ velocity-measurement campaigns (Vinnechenko 1969; Gage 1979; Lilly 1983; Nastrom and Gage 1983; for discussions and references see Schertzer and Lovejoy 1985a; Lovejoy and Schertzer 1986) failed to find evidence for the mesoscale gap anywhere near the designated 1-100-km range. Even though these campaigns did measure velocity fluctuations over various ranges (several meters to thousands of kilometers) with sufficient statistical reliability to eliminate the possibility of a significant gap, the extreme intermittency of the atmosphere and various experimental difficulties has hindered the emergence of a clear overall (large to small scale) statistical picture of the wind field. One way of attempting to overcome the limitation of in situ wind measurements—which we explore later—is to exploit the burgeoning masses of remotely sensed satellite and radar data. Because of the strong (nonlinear) couplings between the various atmospheric fields, any fundamental break in the scaling symmetry in the dynamical (wind) field will be reflected in the latter. Conversely, if the latter are scaling over the observed ranges, we may infer that the symmetry is not broken in the former. The symmetry will be respected unless specific (and strong enough) mechanisms exist to break it. This result follows from the consideration of scale invariance as a symmetry principle. A scaling break in one field would constitute a sufficient mechanism to cause a break in any other strongly dynamically coupled field. The cloud, radiance, and velocity are strongly coupled.

In any case, satellite cloud radiances and radar rain reflectivities are interesting in their own right, and, as argued elsewhere (Lovejoy and Schertzer 1990a; Lovejoy et al. 1992), provide unique datasets for testing new ideas in scaling and multifractals.[2] Indeed, the specific problem of taming the extremely variable atmospheric scaling has already motivated the development of several new data-analysis techniques [e.g., functional box counting (Lovejoy et al. 1987), probability distribution multiple scaling technique (Lavallée et al. 1991a), and the double trace moment technique (Lavallée et al. 1991b; Lavallée 1991].

In this paper, we focus on the scaling properties of various fields related to the liquid water field. The distribution of cloud and rain liquid water is important for our understanding of atmospheric dynamics: it is a fundamental part of the water cycle and (when it reaches the ground) is the basic hydrological field. Section 2 outlines some basic elements of scaling and multifractals. Section 3 then describes the new double trace moment analysis technique, which (in section 4) we apply to remotely sensed atmospheric data for the first time. [Schmitt et al. (1992a) have already applied it to in situ atmospheric temperature measurements.] The datasets used include Landsat, *NOAA-9*, and Meteosat cloud radiances in the visible, thermal infrared, and near-infrared wavelength bands (from approximately 166 m to 4000 km overall). In section 5, we analyze radar reflectivities of rain in both time and space and include a comparison of the latter with global in situ raingage measurements. On all of these datasets, we not only test the scaling (which is generally found to hold quite well), but we also estimate the fundamental universal multifractal exponents characterizing the fields. Finally, in section 6, we briefly indicate how knowledge of these exponents can be used to create (both static and dynamic) multifractal models of the corresponding fields.

---

[1] A related formalism is currently being developed for dealing with scale invariance in astrophysics (see Carter and Henrickson 1991).

[2] It is significant that the first empirical dataset (in meteorology or elsewhere) whose multifractal dimensions were estimated was the radar reflectivity field of rain (Schertzer and Lovejoy 1985b).

2. Multifractal phenomenology of atmospheric turbulence

a. *Multifractal processes*

The multifractal processes discussed here were first developed as phenomenological models of turbulent cascades. In hydrodynamic turbulence, the governing nonlinear dynamical (Navier–Stokes) equations have three properties that lead to the cascade phenomenology: 1) scaling symmetry [invariance under dilations (zooms)], 2) a quantity conserved by the cascade (energy fluxes from large to small scale), and 3) localness in Fourier space (this means that the dynamics are most effective between neighboring scales; direct transfer of energy from large- to small-scale structures is inefficient). Cascade models are relevant in the atmosphere, in general, and in rain and hydrology, in particular, since [as argued in Schertzer and Lovejoy (1987b)], although the full nonlinear partial differential equations governing the atmosphere will be more complex than those of hydrodynamic turbulence, they are nonetheless still likely to respect properties 1-3. To understand this, consider the simplest strongly nonlinear model of rain, the passive-scalar model, which ignores the effect of rain on the dynamics. Virtually the same assumptions are used in numerical weather prediction models. In these models of passive advection of water by a velocity field v, the dynamical equations conserve the flux of energy and of scalar variance (with respective densities ϵ and χ). The injection of these quantities at large scale is assumed to be constant (or at least to be a stationary random process) and then there is the transfer of these to smaller scales (hence the cascade). By considering statistically stationary fields of these quantities, dimensional arguments lead to the laws of Kolmogorov (1941), Obukhov (1949), and Corrsin (1951):

$$E_v(k) \approx \epsilon^{2/3}k^{-5/3}$$

$$E_\rho(k) \approx \xi^{2/3}k^{-5/3}, \qquad (2.1)$$

where $\xi \approx \chi^{3/2}\epsilon^{-1/2}$ and $E_v(k)$ and $E_\rho(k)$ are the power spectra for the velocity and passive-scalar fields, respectively, and k is a wavenumber ($k \approx 1/l$). Here ξ is the flux resulting from the nonlinear interactions of the velocity and the passive scalar. In real space, the equavalent relations are

$$\Delta v(l) \approx \epsilon^{1/3}l^{1/3}$$

$$\Delta\rho(l) \approx \xi^{1/3}l^{1/3}, \qquad (2.2)$$

where $\Delta v(l)$ and $\Delta\rho(l)$ are the characteristic fluctuations of the fields v and ρ at the scale l. These equations should be understood statistically. A straightforward interpretation useful in modeling is to view the scaling $l^{1/3}$ as a power-law filter ($k^{-1/3}$) of $\epsilon^{1/3}$ (Schertzer and Lovejoy 1987b; Wilson et al. 1991; see section 6). These equations are the result of treating passive-scalar advection as a nonlinearly coupled cascade process (for χ and ϵ). As more and more coupled equations are added to account for other interacting fields (such as radiation or water in its various phases), more and more coupled cascades will be obtained. The turbulent and multifractal results presented here are expected to continue to be valid.

There is now a whole series of such phenomenological models: the "pulse-in-pulse" model (Novikov and Stewart 1964), the lognormal model (Kolmogorov 1962; Obukhov 1962; Yaglom 1966), the weighted-curdling model (Mandelbrot 1974), the β model (Frisch et al. 1978), the α model (Schertzer and Lovejoy 1983), the random β model (Benzi et al. 1984), the p model (Meneveau and Sreenivasan 1987), and the continuous and universal cascade models (Schertzer and Lovejoy 1987b). It is now clear that scale-invariant multiplicative processes generically give rise to multifractals and—due to the existence of stable and attractive multifractal generators—to univeral multifractals in which many of the details of the dynamics are unimportant. These results are important in hydrology and geophysics since they show that while geometrical fractals are sufficient to study many aspects of scaling sets, that multifractals (with their statistical exponents) provide the general framework for scaling fields (measures).

In contrast to the well-studied case of hydrodynamic turbulence, the dynamical equations responsible for the distribution of rain and cloud radiances are unknown (the essentially ad hoc parameterizations employed by numerical cloud and weather models are excluded here); the best that can be done at present is to speculate on the appropriate fundamental dynamical quantities analogous to ϵ, ξ. Since a priori there is no obvious reason why the rain rate or cloud radiance fields themselves should be conservative, in analogy with turbulence, we introduce a fundamental field φ_λ that has the conservation property $\langle\varphi_\lambda\rangle$ = constant (independent of scale). The observable (nonconserved) rainfall (or cloud radiance) fluctuations (ΔR_λ) are then given by

$$\Delta R_\lambda \approx \varphi_\lambda^a \lambda^{-H}. \qquad (2.3)$$

Since we have as yet no proper dynamical theory for rain or cloud radiances, we do not know the appropriate fields φ_λ nor the corresponding values of a. In the following discussion, therefore, the simplifying assumption is made that $a = 1$ (changing the value of a corresponds essentially to changing the parameter c_1; see below). With this in mind, the scaling parameter H has a straightforward interpretation: it specifies how far the measured field R is from the conserved field $\varphi : \langle|\Delta R_\lambda|\rangle \approx \lambda^{-H}$. Therefore, H specifies the exponent of the power-law filter (the order of fractional integration) required to obtain R from φ.

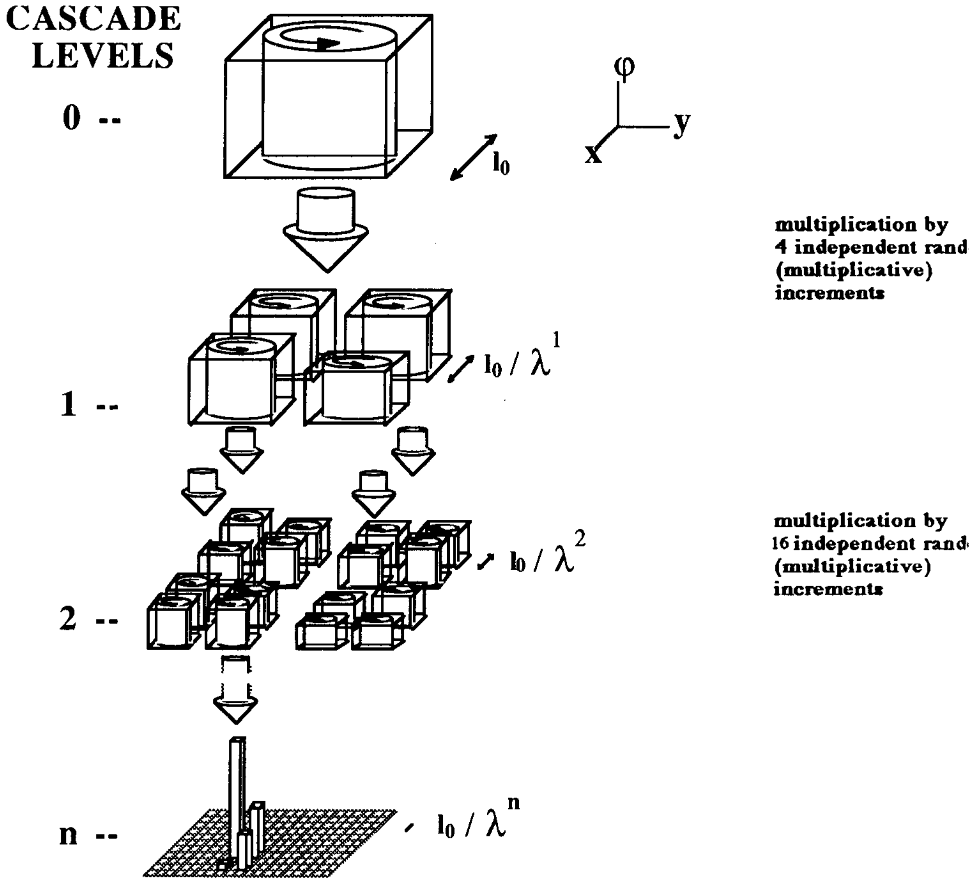

FIG. 1a. A schematic diagram showing a two-dimensional cascade process at different levels of its construction to smaller scales. Each eddy is broken up into four subeddies, transferring a part or all its energy flux to the subeddies. In this process, the flux of the field at large scales multiplicatively modulates the various fluxes at smaller scales; the mechanism of flux redistribution is repeated at each cascade step (self-similarity).

b. Some properties of φ_λ

We now focus our attention on the conserved quantity φ_λ. Early scaling ideas were associated with additive (linear) processes and unique scaling exponents H (which, only in these special cases, were related to unique fractal dimensions by simple formulas). The properties of φ_λ were quite straightforward and were usually understood implicitly. For example, a commonly used (monofractal) process is simple scaling[3], in which φ_λ is simply a scale-invariant random variable; (2.3) then specifies the scaling of the probability distributions of the fluctuations ΔR_λ. When the latter are Gaussian, the resulting process is called *fractional Brownian motion.* [The notion was introduced by Kolmogorov (1940), the expression was coined by Mandelbrot and Van Ness (1968); these are the very special processes used to make the now familiar monofractal mountains.] For meteorological and hydrological applications of simple scaling (especially when the distributions are "long-tailed," involving extreme fluctuations), see Lovejoy (1981) (he used both "R/S" analysis and analysis of probability distributions to estimate $H \approx 0.5$ in radar-estimated rain rates in the horizontal direction), Lovejoy and Mandelbrot (1985), Waymire (1985), Keddem and Chiu (1989), Lovejoy and Schertzer (1989), and Gupta and Waymire (1991).

Turning our attention to (nonlinear) multiplicative processes, some of the properties of φ_λ can be considered that will generically result from cascades. Figures 1a,b illustrate such a discrete multiplicative process for φ_λ: a large structure of characteristic length l_0 with an

---

[3] This type of scaling was first introduced by Lamperti (1962) under the name "semistable." It was called self-similarity by Mandelbrot and Van Ness (1968). This name turned out to be a misnomer, however, since the actual functions were not self-similar but self-affine, and self-similarity is a much wider concept anyway. We use the expression "simple scaling," which contrasts it with the more general and interesting multiple scaling discussed below (see also Lovejoy and Schertzer 1989).

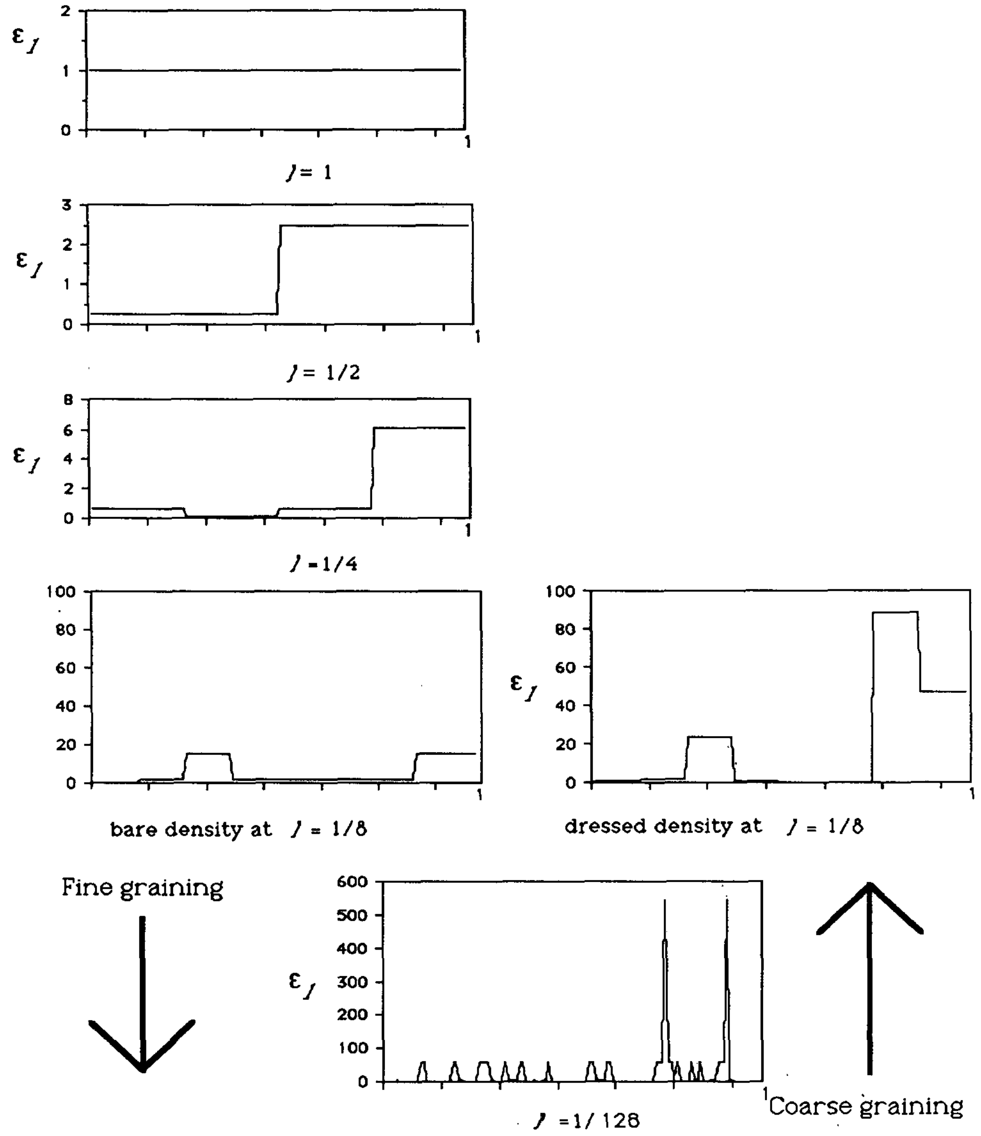

FIG. 1b. A discrete (α model) cascade in one dimension. At each step, the unit interval is broken up into intervals half the size of the previous step and the energy flux density (vertical axis) is multiplied by a random factor. In the a model, there are only two possibilities—a boost or a decrease—with probabilities chosen to respect ensemble conservation $\langle \epsilon_l \rangle = 1$.

initial uniform density φ_0 is broken up (via nonlinear interactions with other structures or through internal instability) into smaller substructures of characteristic length $l_1 = l_0/\lambda_0$ ($\lambda_0 = 2$ is the scale ratio between two construction steps in this particular example), multiplicatively modulating by a (random) factor the flux on each substructure. When the process is repeated (the overall ratio λ is increased; after n iterations, $\lambda = \lambda_0^n$, $l_n = l_0/\lambda_0^n$) larger and larger values of φ_λ appear, concentrated on smaller and smaller volumes. In the small-scale limit, the result is a highly intermittent multifractal measure with singularities of all orders γ distributed on fractal sets with codimension $c(\gamma)$ [Schertzer and Lovejoy (1987b), see the schematic illustration, Fig. 2]. In the range of scales λ between the injection and dissipation of energy (i.e., the scaling regime), the measures on φ_λ have the property

$$\Pr(\varphi_\lambda \geqslant \lambda^\gamma) \approx \lambda^{-c(\gamma)} \qquad (2.4)$$

(equality is to within slowly varying functions of λ such as logs). Therefore, $c(\gamma)$ is the scaling exponent of the probability distribution. When the process is observed on a low-dimensional cut of dimension D (such as the $D = 1$ dimensional simulation shown in Fig. 2), it can often be given a simple geometric interpretation. When

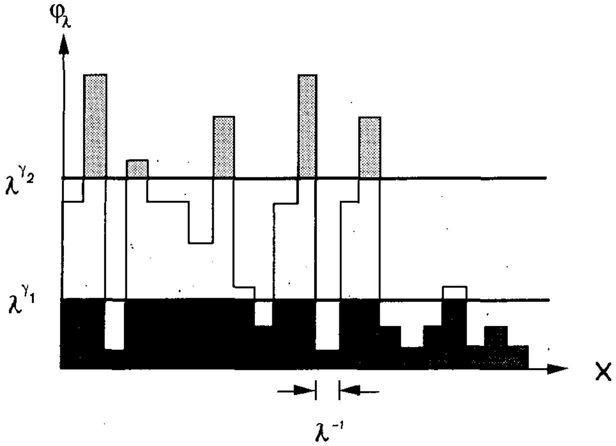

FIG. 2. A schematic diagram showing a multifractal energy flux density φ_λ with smallest resolution λ^{-1} and indicating the exceedance sets corresponding to two orders of singularities γ_1, γ_2.

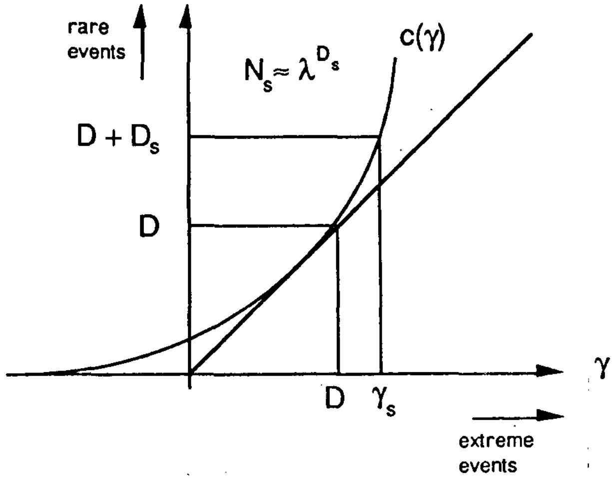

FIG. 3. A schematic diagram showing a typical codimension function for a conserved process ($H = 0$). The lines $c(\gamma) = D$, $\gamma = D$ indicate the limits of the accessible range of singularities for a single realization, dimension D. The corresponding lines for $D + D_s$, where $D_s = \log N_s/\log\lambda$ is the sampling dimension, are also shown. As more and more samples are analyzed, a larger and larger fraction of the probability space of the process is explored, hence revealing more and more extreme (are rare) singularities, up to the value $c(\gamma_s) = D + D_s$.

$D > c(\gamma)$, we may introduce the (positive) dimension function $D(\gamma) = D - c(\gamma)$ which is then the fractal dimension of the set with singularities γ.

This geometric interpretation can be useful in data analysis. For example, consider a dataset consisting of N_s satellite photographs (assumed to be statistically independent realizations from the same statistical ensemble). A single D-dimensional picture ($D = 2$ in this example) will enable us to explore structures with dimension $D \geqslant D(\gamma) \geqslant 0$; structures with $c(\gamma) > D$ [which would correspond to impossible negative values of $D(\gamma)$] will be too sparse to be observed (they will almost surely not be present on a given realization). This restriction on the accessible values of $c(\gamma)$ is shown in Fig. 3; to explore more of the probability space, many photographs will be required. With N_s photographs, the accessible range of singularities can readily be estimated. If each photograph has a range of scales λ (equal to the ratio of the size of the picture to the smallest resolution—the number of pixels on a side), then the sampling dimension is introduced (Schertzer and Lovejoy 1989a; Lavallée et al. 1991): $D_s = \log N_s/\log\lambda$; it is not hard to see (Fig. 3) that the accessible range will be $\gamma < \gamma_s$, with $c(\gamma_s) = D + D_s$.

Codimension $c(\gamma)$ has many other properties that are readily illustrated graphically. A fundamental property that is derived by considering statistical moments (below) is that it must be convex. It must also be tangent to the line $x = y$ (the bisectrix). This is because $\langle \varphi_\lambda \rangle \approx \lambda^{\gamma - c(\gamma)}$ = constant, hence the singularity corresponding to the mean of the process, $\gamma = C_1$, satisfies the fixed point relation $C_1 = c(C_1)$, as indicated in Fig. 4. Thus, C_1 is the codimension of the mean process; if the process is observed on a space of dimension D, it must satisfy $D \geqslant C_1$, otherwise, following the above, the mean will be so sparse that the process will (almost surely) be zero everywhere; it will be "degenerate." Also consider the (nonconserved) ΔR_λ; it is obtained from φ_λ by multiplication by λ^{-H}. Wherever $\varphi_\lambda = \lambda^\gamma$, we have $\Delta R_\lambda = \lambda^{\gamma - H}$; that is, by the translation of singularities by $-H$ (see Fig. 5). Finally, since $c(\gamma)$ is convex with fixed point C_1, it is possible (see Fig. 6) to define the degree of multifractality (α) by the (local) rate of change of slope at C_1, its radius of curvature $R_c(C_1)$:

$$R_c(C_1) = 2^{2/3}\alpha C_1. \tag{2.5}$$

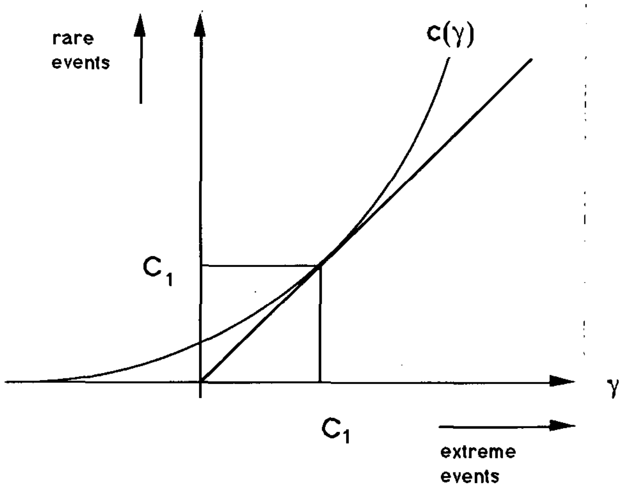

FIG. 4. The same as in Fig. 3 but showing the fixed point $C_1 = c(C_1)$, the singularity corresponding to the mean of the process. The diagonal line is the bisectrix [$\gamma = c(\gamma)$].

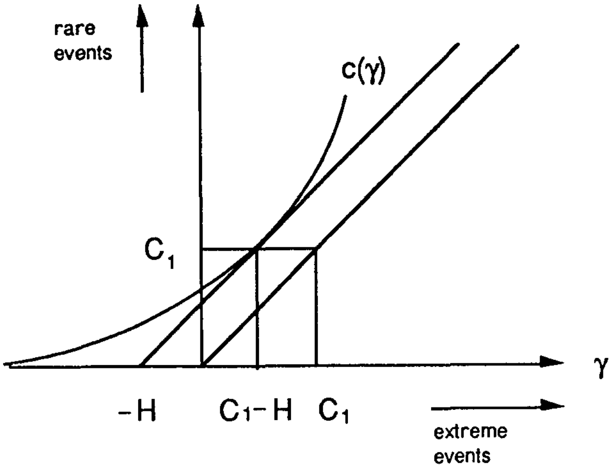

FIG. 5. Same as Fig. 4 but for a nonconserved process. All the singularities are shifted by $-H$.

In universal multifractals, this local description obtained by a Taylor expansion gives all the relevant parameters for a global description of the $c(\gamma)$ function, and we find an upper bound (maximum degree of multifractality) $\alpha = 2$, yielding a parabola. The $\alpha = 0$ case is the monofractal extreme [called the β model, Frisch et al. (1978)] whose singularities all have the same fractal dimension (see Fig. 6).

Rather than specifying the statistical properties via the scaling of probabilities $c(\gamma)$, it can (equivalently) be specified by the scaling of the statistical moments. Consider the qth order statistical moments $\langle \varphi_\lambda^q \rangle$. We can now define the multiple-scaling exponent $K(q)$:

$$\langle \varphi_\lambda^q \rangle \approx \lambda^{K(q)}, \quad \lambda > 1. \tag{2.6}$$

In parallel to this turbulent multifractal formalism, Hentchel and Procaccia (1983), Grassberger (1983), Halsey et al. (1986), and others elaborated a strange attractor formalism for dealing with multifractal probability measures in low-dimensional phase spaces. They were primarily interested in the fractal dimensions of geometric sets associated with singularities of measures (rather than densities of measures). This strange attractor notation is related to the turbulence notation as follows:

$$f_D(\alpha_D) = D - c(\gamma); \quad \alpha_D = D - \gamma. \tag{2.7}$$

In turbulence, interest lies in stochastic processes defined on (infinite-dimensional) probability spaces, hence the intrinsic (D independent) notation.

Parameters $K(q)$ and $c(\gamma)$ are related by the following Legendre transformations (Parisi and Frisch 1985):

$$K(q) = \max_\gamma[q\gamma - c(\gamma)],$$
$$c(\gamma) = \max_q[q\gamma - K(q)], \tag{2.8}$$

which relate points on the $c(\gamma)$ function to tangencies on the $K(q)$ function and vice versa; $\gamma = K'(q)$, $q = c'(\gamma)$. For example, a quantity that will be useful below in estimating the multifractal parameters of radiances and reflectivities is the sampling moment q_s, which is the maximum-order moment that can be accurately estimated with a finite sample. Recalling that the maximum accessible order of singularity was $\gamma_s = c^{-1}(D + D_s)$, $q_s = c'(\gamma_s)$ is obtained. Figure 7 shows a schematic of $K(q)$; for conserved fields, $C_1 = K'(1)$ is given (i.e., $q = 1$ corresponds to $\gamma = C_1$), the corresponding radius of curvature is $R_K(1) = (1 + C_1^2)^{2/3}(C_1\alpha)^{-1}$. The functions for the corresponding nonconserved fields ($H \neq 0$) are obtained by $\gamma \rightarrow \gamma - H$, $K(q) \rightarrow K(q) - Hq$.

In summary, this local characterization of the behavior of multifractals near the mean involves the three parameters (H, C_1, α), respectively, characterizing the deviation of the observed field from the conserved field φ, the sparseness of the latter, and the degree of multifractality.

Finally, a distinction must be made between the "bare" and "dressed" multifractal properties (Schertzer and Lovejoy 1987). The bare properties are those that have been discussed above, they correspond to the construction of the process over a finite range of scales λ. In contrast, the dressed quantities are obtained by integrating (averaging) a completed cascade over the corresponding scale. Experimentally measured quantities are generally dressed since geophysical sensors typically have resolutions that are much lower than the scale below which the fields they are measuring become homogeneous (in the atmosphere, the latter is usually of the order of 1 mm or less). The dressed quantities

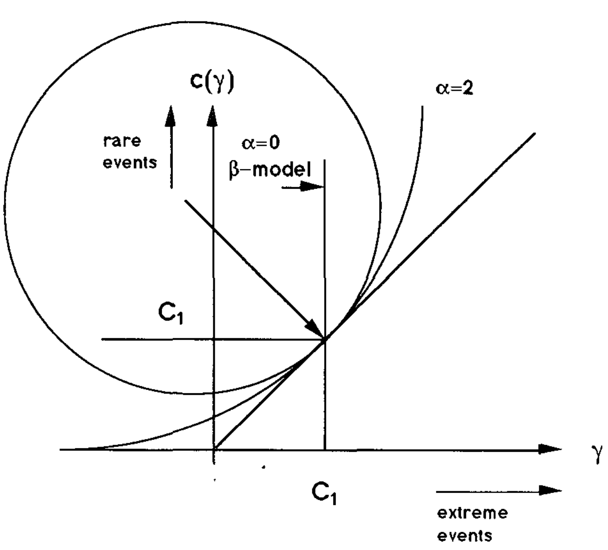

FIG. 6. Same as Fig. 4 but showing the radius of curvature ($=2^{2/3}C_1\alpha$) at the fixed point that locally defines α. For comparison, the two extreme universal multifractals are also shown, corresponding to $\alpha = 0$ (the β model), $\alpha = 2$ (the lognormal model).

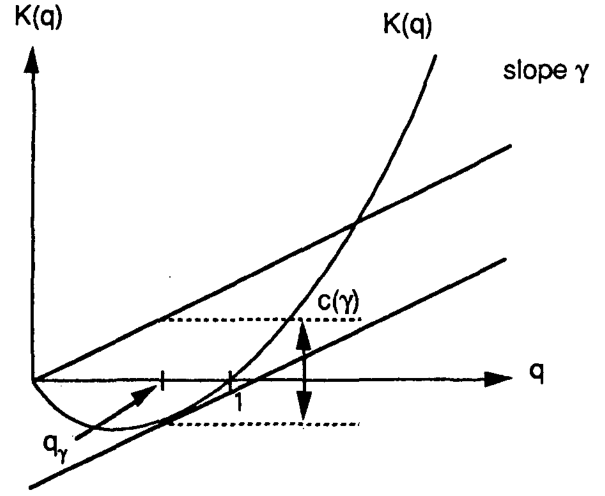

FIG. 7. The $K(q)$ curves corresponding to the $c(\gamma)$ curves in Fig. 6 are shown. Also shown is a typical tangent whose slope $K'(q) = \gamma_q$ provides the one-to-one correspondence between orders of singularities and moments.

generally display an extreme, "hard" behavior involving divergence of high-order statistical moments (see in particular Schertzer and Lovejoy 1992). Specifically, for averages over observing sets with dimension D, there is a critical-order moment q_D [and corresponding order of singularity $\gamma_D = K'(q_D)$] such that

$$\langle \varphi_\lambda^q \rangle = \infty, \quad q \geq q_D, \tag{2.9}$$

where q_D is given by the following equation:

$$K(q_D) = (q_D - 1)D. \tag{2.10}$$

c. *Universal multifractals*

The above discussion is quite general and at this level, it has the unpleasant consequence that an infinite number of scaling parameters [the entire $c(\gamma)$, $K(q)$ functions] will be required to fully specify the multiple scaling of our field. Fortunately, real physical processes will typically involve both nonlinear "mixing"[4] (Schertzer et al. 1991) of different multifractal processes, as well as a "densification"[5] (Schertzer and Lovejoy 1987) of the process leading to a continuum of scales (rather than just the discrete scales indicated in Figs. 1a,b. Either of these mechanisms is sufficient so that the above H, C_1, α description becomes global; the following universal multifractal functions are obtained:

$$c(\gamma - H) = \begin{cases} C_1\left(\dfrac{\gamma}{C_1\alpha'} + \dfrac{1}{\alpha}\right)^{\alpha'}, & \alpha \neq 1 \\ C_1 \exp\left(\dfrac{\gamma}{C_1} - 1\right), & \alpha = 1 \end{cases} \tag{2.11}$$

$$K(q) + qH = \begin{cases} \dfrac{C_1}{\alpha - 1}(q^\alpha - q), & \alpha \neq 1 \\ C_1 q \log(q), & \alpha = 1 \end{cases}$$
$$(\text{for } 0 \leq \alpha \leq 2,\ q \geq 0). \tag{2.12}$$

The multifractality parameter α is the Levy index and indicates the class to which the probability distribution belongs. There are actually five qualitatively different cases. The case $\alpha = 2$ corresponds to lognormal[6] multifractals, the case $1 < \alpha < 2$ corresponds to (log) Levy processes with unbounded singularities, and $\alpha = 1$ corresponds to log-Cauchy multifractals. These three cases all are "unconditionally hard" multifractals, since for any D, divergence of moments will occur for large enough q (q_D is always finite). When $0 < \alpha < 1$, (log) Levy processes are given with bounded singularities. By integrating (smoothing) such multifractals over an observing set with large enough dimension D, it is possible to tame all the divergences yielding "soft" behavior, these multifractals are only conditionally "hard." Finally, $\alpha = 0$ corresponds to the most popular and well-known monofractal β model (Novikov and Stewart 1964; Mandelbrot 1974; Frisch et al. 1978). A more detailed discussion about these five cases and in particular about the generators of the Levy variables can be found in Schertzer et al. (1988), Fan (1989), and Schertzer and Lovejoy (1989b) [see also Lovejoy and Schertzer (1990b, 1991) for some applications and review]. Universal multifractals have been empirically found in both turbulent temperature and wind data (Schmitt et al. 1992a,b). They have also recently found applications in high-energy physics (Brax and Peschanski 1991), as well as oceanography (Tessier et al. 1992a), earthquakes (Beltrami et al. 1991), and landscape topography (Lavallée et al. 1991b). The first empirical estimates of C_1, α in cloud radiances are discussed in Lovejoy and Schertzer (1990b) (see also Gabriel et al. 1988) and for rain reflectivities (Seed 1989).

Using the universal multifractal formulas above, some of the results discussed earlier may be expressed in simpler form. Formulas that will prove useful below are for q_s (the maximum-order moment that can be

---

[4] By keeping the total range of scale λ fixed and finite, we may mix (by multiplying them) independent processes of the same type, preserving certain characteristics (e.g., the variance of the resulting processes).

[5] Introducing more and more intermediate scales in a given multiplicative process.

[6] This is nearly the same as the lognormal multiscaling model of turbulence proposed by Kolmogorov (1962) and Obukhov (1962), except that the latter missed the essential point about the divergence of high-order moments, thinking in terms of pointwise processes.

reliably estimated with a finite sample), and q_D, the critical order for divergence [obtained by solving (2.13b) for q_D]:

$$q_s = \left(\frac{D + D_s}{C_1}\right)^{1/\alpha} \qquad (2.13a)$$

$$\frac{C_1}{\alpha - 1}\,\frac{q_D^\alpha - q_D}{q_D - 1} = D. \qquad (2.13b)$$

Equation (2.13a) is valid only for $q_s < q_D$.

Both of these critical moments are associated with "multifractal phase transitions" (Schertzer et al. 1992b), and algebraic probabilities (finite q_D) are considered a basic characteristic of self-organized criticality (Bak et al. 1988).

3. The double trace moment technique

a. Basic ideas

We have argued that atmospheric fields are multifractal, involving an infinite number of scaling exponents [the functions $c(\gamma)$, $K(q)$], but that due to universality, the latter may be characterized by the three basic parameters (H, C_1, α). In this section, we discuss a way in which this idea may be tested and the parameters estimated.

The physics literature is now replete with different methods developed for estimating multifractal parameters. Unfortunately, the great majority of these have been designed for the particularly "calm" multifractals associated with strange attractors, a few for the slightly less calm "microcanonical" multifractals,[7] but virtually none for the general ("canonical") multifractals involving the occasional "hard" singularities discussed earlier. When applied to turbulent and/or geophysical data involving extreme variability, they will have limited accuracy. A final limitation on their accuracy comes from the fact that they have attempted to estimate an infinite number of parameters with finite datasets [the entire $c(\gamma)$, $K(q)$ function, each value of which is a scaling exponent]. Now a simple technique is described that overcomes these problems by exploiting the universality to estimate C_1 and α directly; $c(\gamma)$, $K(q)$ are then obtained using (2.11) and (2.12). Then H is estimated by combining the C_1 and α estimates with the scaling exponent of the energy spectrum (section 3b).

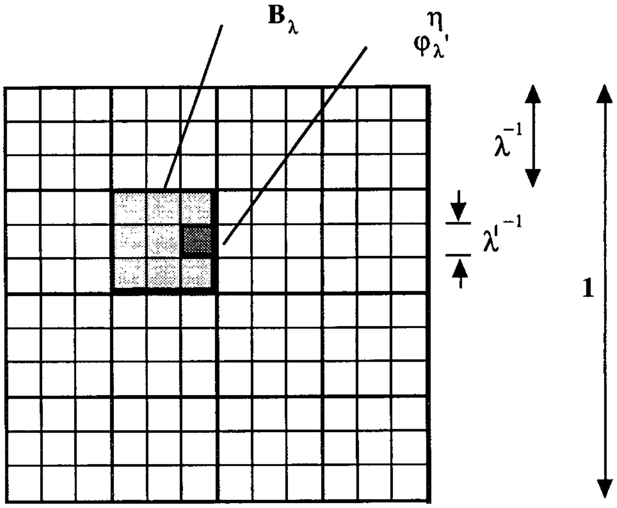

FIG. 8. A schematic diagram illustrating the different averaging scales used in the double trace moment technique.

Consider the conserved ($H = 0$) multifractal flux density at (fine) resolution λ' [the ratio of the outer (largest) scale of interest to the smallest scale of homogeneity]. [For scales smaller than the scale of homogeneity the field is homogeneous. Here we take λ' as the smallest scale known (the pixel scale) for the analyzed field.] The (dressed) flux over an observing set B_λ corresponds to a single lower-resolution pixel with dimension D and resolution $\lambda < \lambda'$ is simply an integral over the density

$$\Pi_{\lambda'}(B_\lambda) = \int_{B_\lambda} \varphi_{\lambda'} d^D x. \qquad (3.1)$$

We may now define the qth-order trace moments (Schertzer and Lovejoy[8] 1987b) by summing $\Pi_{\lambda'}^q(B_\lambda)$ over each individual realization—this yields a partition function—[each satellite picture, covering the region A, has λ^D disjoint covering sets B_λ that are summed in (3.2), see the schematic illustration, Fig. 8 with $\eta = 1$], and then ensemble averaging over all the realizations,

$$\mathrm{Tr}_\lambda(\varphi_{\lambda'})^q = \Big\langle \sum_i \Pi_\lambda^q(B_{\lambda,i})\Big\rangle \approx \lambda^{K(q)-(q-1)D}, \qquad (3.2)$$

where the sum is over all the i "balls" $B_{\lambda,i}$ needed to cover A. This formula will break down for moments $q > q_D$ and (when finite samples are used to estimate the ensemble average) when $q > q_s$. Although it allows the determination of $K(q)$ (at least for small enough q), and hence in principle the determination of C_1, α [via (2.12)], this method will involve ill-conditioned nonlinear regressions [$K(q)$ versus q]. The double trace moment (DTM) technique (Lavallée et al. 1991b; Lavallée 1991) avoids this problem by generalizing the

---

[7] This is true for example of approaches bases on partition functions and moments (Halsey et al. 1986), single-scale histograms (Atmanspacher et al. 1989; Paladin and Vulpiani 1987), multipliers (Chhabra and Sreenivasan 1991), and wavelets (Bacry et al. 1989).

[8] Although the formalism above was developed in Schertzer and Lovejoy (1987a,b), essentially the same method was empirically applied to rain in Schertzer and Lovejoy (1985).

trace moment; it introduces a second moment η by transforming the high-resolution field $\varphi_{\lambda'} \rightarrow \varphi_{\lambda'}^{\eta}$. This transforms the flux Π into an "η flux" $\Pi^{(\eta)}$:

$$\Pi_{\lambda}^{(\eta)}(B_\lambda) = \int_{B_\lambda} \varphi_{\lambda'}^{\eta} d^D x. \tag{3.3}$$

The double trace moment can then be defined as

$$\mathrm{Tr}_\lambda(\varphi_{\lambda'}^{\eta})^q = \langle \sum_i [\Pi_{\lambda'}^{(\eta)}(B_{\lambda,i})]^q \rangle \approx \lambda^{K(q,\eta)-(q-1)D}, \tag{3.4}$$

where we have introduced the (double) exponent $K(q, \eta)$, which reduces to the usual exponent when $\eta = 1$: $K(q, 1) = K(q)$.

The entire transformation from single to double trace moments can be summarized in the following formulas (where the prime indicates transformed, double trace quantities, not differentiation):

$$\gamma \rightarrow \gamma' = \eta\gamma - K(\eta) \tag{3.5a}$$

$$c(\gamma) \rightarrow c'(\gamma') = c(\gamma) \tag{3.5b}$$

$$q \rightarrow q' = \frac{q}{\eta} \tag{3.5c}$$

$$K(q) \rightarrow K'(q') = K(q, \eta) = K(\eta q') - q'K(\eta). \tag{3.5d}$$

Note the fine point in the above is that due to the integration, we require dressed rather than bare quantities, hence, the dressed singularities (3.5a) transform with an extra term $[-K(\eta)]$, which arises since the dressing operation enforces conservation of the η flux.

The real advantage of the DTM technique becomes apparent when it is applied to universal multifractals (Lavallée 1991), since the following transformations of C_1 are obtained:

$$C_1\left(= \left.\frac{dK}{dq}\right|_{q=1} \right) \rightarrow C_1'\left(= \left.\frac{dK'}{dq'}\right|_{q'=1} \right) = C_1\eta^\alpha. \tag{3.6}$$

Therefore, $K'(q') = K(q, \eta)$ has a particularly simple dependence on η:

$$K(q, \eta) = \eta^\alpha K(q). \tag{3.7}$$

Therefore, α can be estimated on a simple plot of $\log K(q, \eta)$ versus $\log \eta$ for fixed q. By varying q, our statistical accuracy is improved. Finally, note that due to (3.5d), whenever $\max(q\eta, q) > \min(q_s, q_D)$, the above relation will break down; $K(q, \eta)$ will become independent of η. For more details on the double trace moment, see Lavallée et al. (1991b) and Lavallée (1991). We shall see that effective exploitation of the above involves a bootstrap procedure in which the well-estimated low q, η exponents are used to estimate α, C_1, and then (2.13a) and (2.13b) can be used to predict the range of reliable estimates.

b. Estimating H

We have seen that in multiplicative processes, it is convenient to isolate an underlying conserved quantity that has basic physical significance; in turbulence, it was the energy flux to smaller scales, in rainfall, it was denoted by φ and related to the rain fluctuations via (2.2). In terms of the scaling, conservation means $\langle \varphi_\lambda \rangle$ = constant (independent of λ), hence $K(1) = 0$. If we consider the energy spectrum of φ_λ, it is of the form $k^{-\beta}$ with[9] $\beta = 1 - K(2)$; that is, the spectrum is always less steep than a $1/f$ noise. [The difference is often not great since $K(2)$ is usually small: $= C_1(2^\alpha - 2) \times (\alpha - 1)^{-1}$ and $0 \leqslant \alpha \leqslant 2$.]

The reason for dwelling on this is that it illustrates a basic point common to many geophysical fields, namely, their spectra have $\beta > 1$, hence they cannot be stationary processes, they must be (fractionally) differentiated[10] by order $-H$ (the spectra must be power-law filtered by k^H) to become stationary. For rain and clouds, this will mean removing the λ^{-H} term in order to obtain the stationary φ_λ from the nonstationary ΔR_λ. The importance of this for analysis has long been realized; for example, standard geophysical statistics use variograms rather than autocorrelation functions to avoid convergence problems when $\beta > 1$. [In time series, we analyze the differences (finite derivatives) rather than the series itself.] The same considerations apply to the use of the DTM technique. Figure 9 (from Lavallée 1991) shows the result when a simulated conserved process is fractionally integrated and differentiated by varying amounts: as long as we differentiate (filter by k^H with $H > 0$) we obtain stable and accurate estimates of both C_1 and α. However, when we fractionally integrate ($H < 0$), we only recover α; C_1 is not accurately determined. [Note that in many geophysical fields, the absolute value of the field may not be important. It may be sufficient to only consider fluctuations, hence, we may put the mean equal to 0 by setting the 0th Fourier component equal to 0. In some cases, this component may be important and must be carefully dealt with in real space—see Schertzer and Lovejoy (1991, appendix B.2).] This figure also clearly indicates that as long as the spectrum is less steep than the underlying conserved process [$\beta < 1 - K(2)$], C_1 can be recovered. From the C_1, α estimated this way, we can determine $K(2)$ from (2.10) and hence the β of the conserved process, and infer the amount of fractional integration required to go from the underlying conserved process to the observed nonconserved process. [In the case of turbulence, it is not

---

[9] This formula is a consequence of the fact that the energy spectrum is the Fourier transform of the autocorrelation function, which is a second-order moment.

[10] See Schertzer and Lovejoy (1991b, appendix B.2) for more discussion of fractional derivatives and integrals.

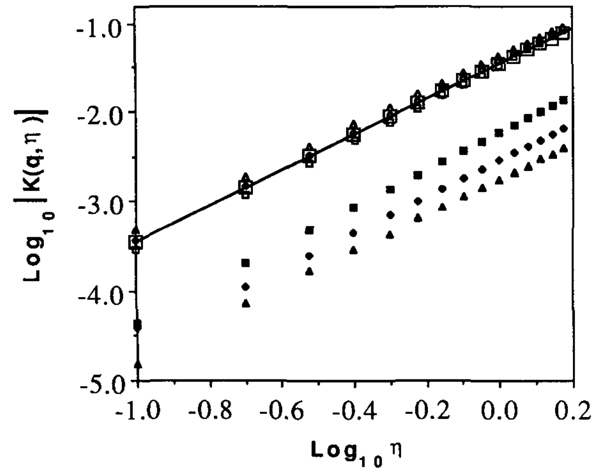

FIG. 9. The $\log[|K(q,\eta)|]$ versus $\log(\eta)$ with $\alpha = 2$ (lognormal), $C_1 = 0.15$, and $D = 2$ is given for $q = 0.5$. The curve of the stationary processes (big hollow square) is compared to those of the same processes after fractional differentiation (white symbols, $H = -2, -1$, and -0.5 from top to bottom). The fractional differentiation and integration does not affect the estimate of α (all the slopes are parallel), but fractional integration leads to biased estimates of C_1 (the curves with black symbols are all shifted downwards compared with the theoretical stationary processes shown by the line).

necessary to infer the relation since it is given by dimensional analysis from known dynamical quantities. For rainfall and cloud radiances, the corresponding dynamical (partial differential) equations are unknown, as well as their conserved quantities, so that at present this type of empirical inference is unavoidable.] Writing β for the spectral slope of the observed process, the order of fractional integration required to go from the conserved process to the nonconserved (observed) process is therefore given by

$$H = \frac{\beta - 1 + K(2)}{2} = \frac{\beta - 1}{2} + \frac{C_1(2^\alpha - 2)}{2(\alpha - 1)}. \tag{3.8}$$

As a final comment before turning to the actual data analysis, a shortcut is described that in many cases enables us to avoid the use of Fourier space. In one dimension we have recalled that replacing the time series by its differences is approximately the same as multiplying by k in Fourier space. (This will not be exactly true at the highest frequencies corresponding to the resolution the series.) To generalize this to two (or more) dimensions, one possibility is to use a finite-difference Laplacian. This multiplies by $|\mathbf{k}|^2$ in Fourier space, hence the spectrum by $|\mathbf{k}|^4$; although this is quite drastic, it apparently works fairly well. Differencing the experimental data also removes the problem of physical quantities that are defined only to within additive constants. This also has the advantage that it removes any (unknown) additive constant that would mask the scaling behavior. Denoting the modulus of the gradient of the rain (or radiance) field by $|\nabla R|$, we have

$$|\nabla R(x, y)| = \left[\left(\frac{\partial R}{\partial x}\right)^2 + \left(\frac{\partial R}{\partial y}\right)^2\right]^{1/2}, \tag{3.9}$$

which can be approximated by the finite difference

$$|\nabla R(i,j)| = \{[R(i+1,j) - R(i-1,j)]^2 + [R(i,j+1) - R(i,j-1)]^2\}^{1/2} \tag{3.10}$$

with $\Delta x = \Delta y = 1$. The index i and j are, respectively, the horizontal and vertical coordinates. The finite-difference operations are affected without privileging any particular direction; problems related to anisotropy are neglected. In the same manner the Laplacian,

$$|\nabla^2 R(x, y)| = \left|\frac{\partial^2 R}{\partial x^2} + \frac{\partial^2 R}{\partial y^2}\right|, \tag{3.11}$$

is approximated by

$$|\nabla^2 R(x, y)| \approx \left|\frac{1}{4}[4R(i,j) - R(i+1,j) - R(i-1,j) - R(i,j+1) - R(i,j-1)]\right|. \tag{3.12}$$

4. Empirical analysis of the spatial structure of clouds and rain

a. *Discussion*

The direct estimation of the spatial and/or temporal distribution of water in any of its phases in the atmosphere is difficult and limited to in situ measurements. Many of the current measurement difficulties could be overcome if we were able to model the extreme variability of water in the atmosphere because then we would be able to infer and simulate what different (both remote and in situ) sensors would measure. For example, one could simulate the estimation of areal rainfall from sparse raingage networks, and one could perform proper radiative transfer calculations to model (Davis et al. 1991) what would be seen from a satellite at various wavelengths or what a weather radar would measure [see Lovejoy and Schertzer (1990b,c) for discussion of various fractal and multifractal effects on radar reflectivities]. A primary goal of multifractal analysis is precisely to provide the information necessary to calibrate such models. The difficulties associated with direct measurement of liquid water have been mentioned; however, many of the fields dynamically coupled with the latter are relatively easy to measure. In this spirit, daily rainfall accumulations on a global network, radar scans during rainstorms, and satellites images (visible, near infrared, and thermal infrared) were all studied. In the following subsections, analyses of various fields associated with rain and

TABLE 1. The characteristics of the different satellite images analyzed.

Location	Satellite	Sensor	Wavelength (μm)	Resolution	Picture size (km)
Tropical Pacific	Landsat	MSS	0.49–0.61	166 m*	512 × 512 89 km
Atlantic west of Spain	Meteosat	visible channel	0.4–1.1	8 km**	512 × 512 4000 km
Atlantic west of Spain	Meteosat	infrared channel	10.5–12.5		
Atlantic east of Florida	*NOAA-9*	AVHRR channel 1	0.5–0.7	1.1 km	512 × 512 550 km
		AVHRR channel 2	0.7–1.0		
		AVHRR channel 3	3.6–3.9		
		AVHRR channel 4	10.4–11.1		
		AVHRR channel 5	11.4–12.2		

* The resolution of the sensor is 83 m, but this resolution had to be degraded in order to avoid certain problems discussed in the text.

** The visible-channel data was originally at a slightly higher resolution and was resampled on a 8-km grid.

clouds are compared in an effort to achieve a better characterization of the fields associated with atmospheric water.

b. *The horizontal scaling properties of cloud radiances*

Scale invariance has already been discussed as an important atmospheric symmetry principle. If over the range in which most of the interactions with the solar and blackbody radiation fields occur, it applies to the distribution of water in the atmosphere, then the radiance fields will also be scale invariant over the corresponding range. (That is, they will not break the scaling symmetry. Formally, this is because the radiative transfer equations have no characteristic length associated with them.) Although the multifractal parameters of the radiation fields will be nontrivially related to those of the liquid water field, they will still give valuable information about the limits to scaling and anisotropic scaling (Pflug et al. 1993; Lovejoy et al. 1992) and the relation between cloud and radiation fields.

Because of the ready availability of high-quality satellite data and our desire to obtain a resolution-independent characterization of the satellite data, images emanating from several different satellites and sensors, which are summarized in Table 1, are analyzed.

The first analysis performed was the estimation of the (isotropic) energy (power) spectrum, which is the modulus squared of the Fourier amplitudes integrated over all angles in Fourier space and ensemble averaged over all realizations of the process. As usual, the ensemble averaging was approximated by averaging over all the available samples with the same wavelength bands and resolution. Figure 10 shows the results for the satellite images whose frequency bands are indicated in Table 2. For all the spectra, reasonable scaling behavior is observed for the entire range accessible to each satellite. The following results are obtained (from bottom to top): Landsat (visible) $\beta = 1.7$; Meteosat (visible) $\beta = 1.4$; Meteosat (infrared) $\beta = 1.7$; *NOAA-9* (channels 1–5) $\beta = 1.67$, 1.67, 1.49, 1.91, and 1.85. The variations in the exponents have both statistical and systematic origins. First, spectral exponents of intermittent data are notoriously difficult to estimate, requiring very large sample sizes. Second, the spectral bands vary from one satellite to another. Even if they are labeled as being in the same group (visible, near infrared, thermal infrared), they are not completely coincident, as can be seen in Table 2. Roughly speaking, the radiative transfer in the visible is dominated by scattering, in the near infrared it combines both scattering with absorption and emission, while in the thermal infrared it is dominated by absorption and thermal emission. Since these radiative transfer processes are quite different, some systematic variation in the power spectra is expected. These results are good

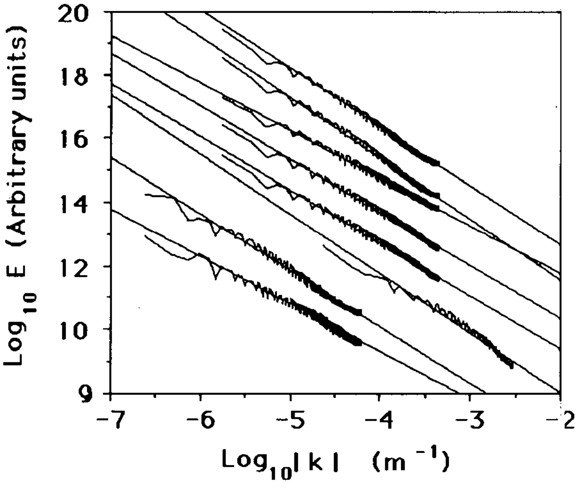

FIG. 10. Average power spectrum for the satelites images grouped according to the satellite and the frequency range of the images (from bottom to top): Landsat (visible) $\beta = 1.7$, Meteosat (visible) $\beta = 1.4$, Meteosat (infrared) $\beta = 1.7$, and *NOAA-9* (channels 1–5) $\beta = 1.67$, 1.67, 1.49, 1.91, and 1.85.

evidence that the basic scaling is respected over the range of approximately 200 m to 2000 km.

The DTM analysis was done on each group of images considering each scene as a separate realization. In Fig. 11, $\log[\mathrm{Tr}_\lambda(\varphi_{\lambda'}^{\eta})^q]$ versus $\log(\lambda)$ is shown for several values of η for the Landsat images. The same plot is shown in Fig. 12 for Meteosat images in the visible and infrared channels. The corresponding graph (Fig. 13) is also shown for all the channels of *NOAA-9*. As expected from the spectral analysis, these graphs are nearly linear over all the accessible range. This is another confirmation that scaling is obeyed over the observed range. Therefore, from here on, we will concentrate on the determination of the universal parameters.

From these $\log[\mathrm{Tr}_\lambda(\varphi_{\lambda'}^{\eta})^q]$ versus $\log(\lambda)$ curves, the slope, and hence $k(q, \eta)$, was obtained. We then plot $\log K(q, \eta)$ versus $\log\eta$, from whose slope we deduce the universal parameter α and from whose intercept with the line $\log\eta = 0$ we estimate C_1. In Fig. 14, a typical result for our analysis is shown. In this case, the analysis was performed on the gradient of one image and the values $\alpha = 1.3$ and $C_1 = 0.1$ were obtained. The deviation from linear behavior at high values of η is due to undersampling problems (2.13a); this problem should occur for values of $\max(q\eta, \eta) = \min(q_s, q_D) \approx q_s$ ($q_D > 50$ for $D = 2$), which in this case (since only one image is used) is estimated to be

$$q_s = \left(\frac{D}{C_1}\right)^{1/\alpha} = \left(\frac{2}{0.1}\right)^{1/1.3} \approx 10, \qquad (4.1)$$

which is close to the value estimated directly on the graph: the straight-line behavior breaks down at $\eta \sim 5$ ($q = 2$ here). As expected, this is roughly where the curve becomes horizontal.

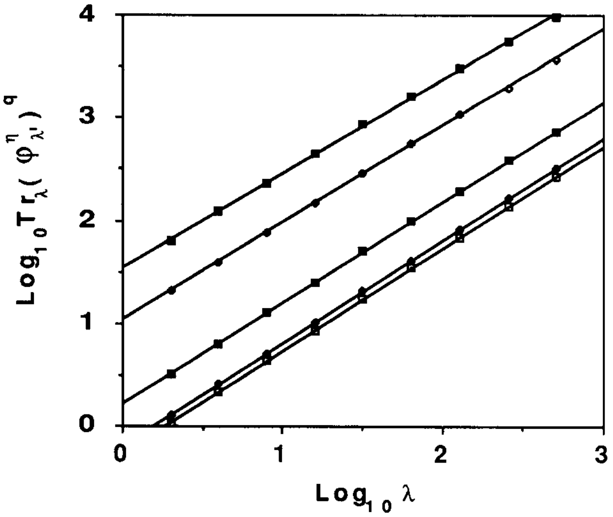

FIG. 11. The $\log[\mathrm{Tr}_\lambda(\varphi_{\lambda'}^{\eta})^q]$ versus $\log(\lambda)$ for several values of η (from top to bottom, $\eta = 3.2, 2.5, 1.2, 0.35$, and 0.15) using $q = 0.5$ for the gradient of three images taken by Landsat.

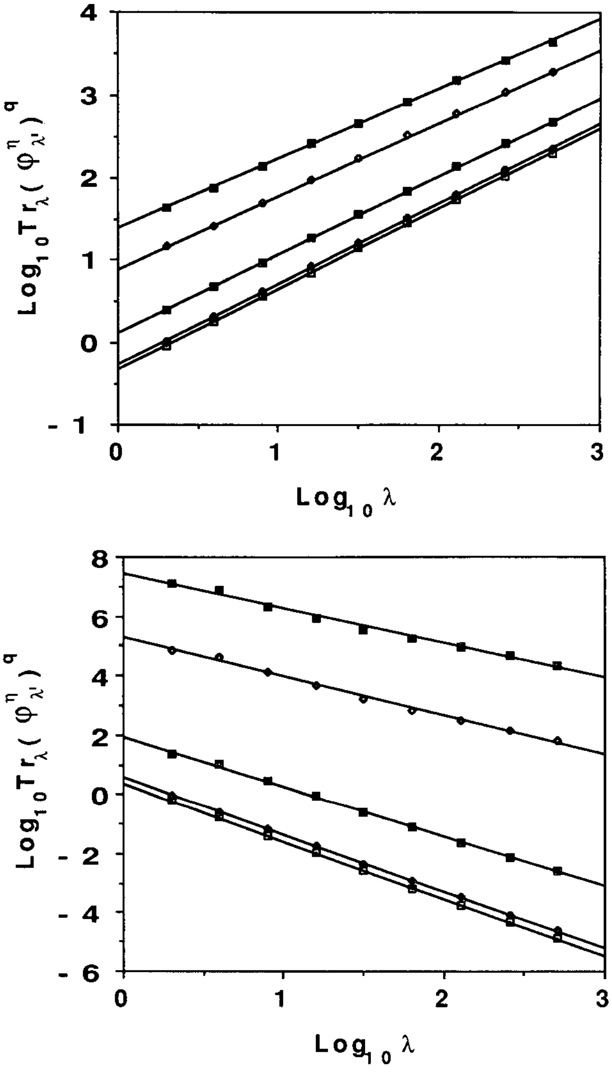

FIG. 12. (a) $\log[\mathrm{Tr}_\lambda(\varphi_{\lambda'}^{\eta})^q]$ versus $\log(\lambda)$ for several values of η (from top to bottom, $\eta = 3.2, 2.5, 1.2, 0.35$, and 0.15) using $q = 0.5$ for the gradient of images taken by Meteosat in the visible. (b) Same as (a) but for the infrared channel and using $q = 2.0$.

For the reason given in section 3b (i.e., the possibility of nonconserved fields), the modulus of the gradient and the modulus of the Laplacian of the radiance fields are analyzed. As expected, both methods always gave similar results, so in order to assure the reader of this fact, the resulting $\log(|K(q, \eta)|)$ versus $\log(\eta)$ is reproduced for the modulus of the gradient and the Laplacian of one of the analyzed images (Fig. 15). From here on, all the analyses will be performed using the gradient except where stated otherwise.

Figure 16 shows a plot of $\log[|K(q, \eta)|]$ versus $\log\eta$ for all the images taken in the visible-wavelength channel. It can be seen that even if the images cover different scales and have slightly different wavelengths, the different satellites agree well. Here $\alpha = 1.2$ and $C_1 = 0.0.8$

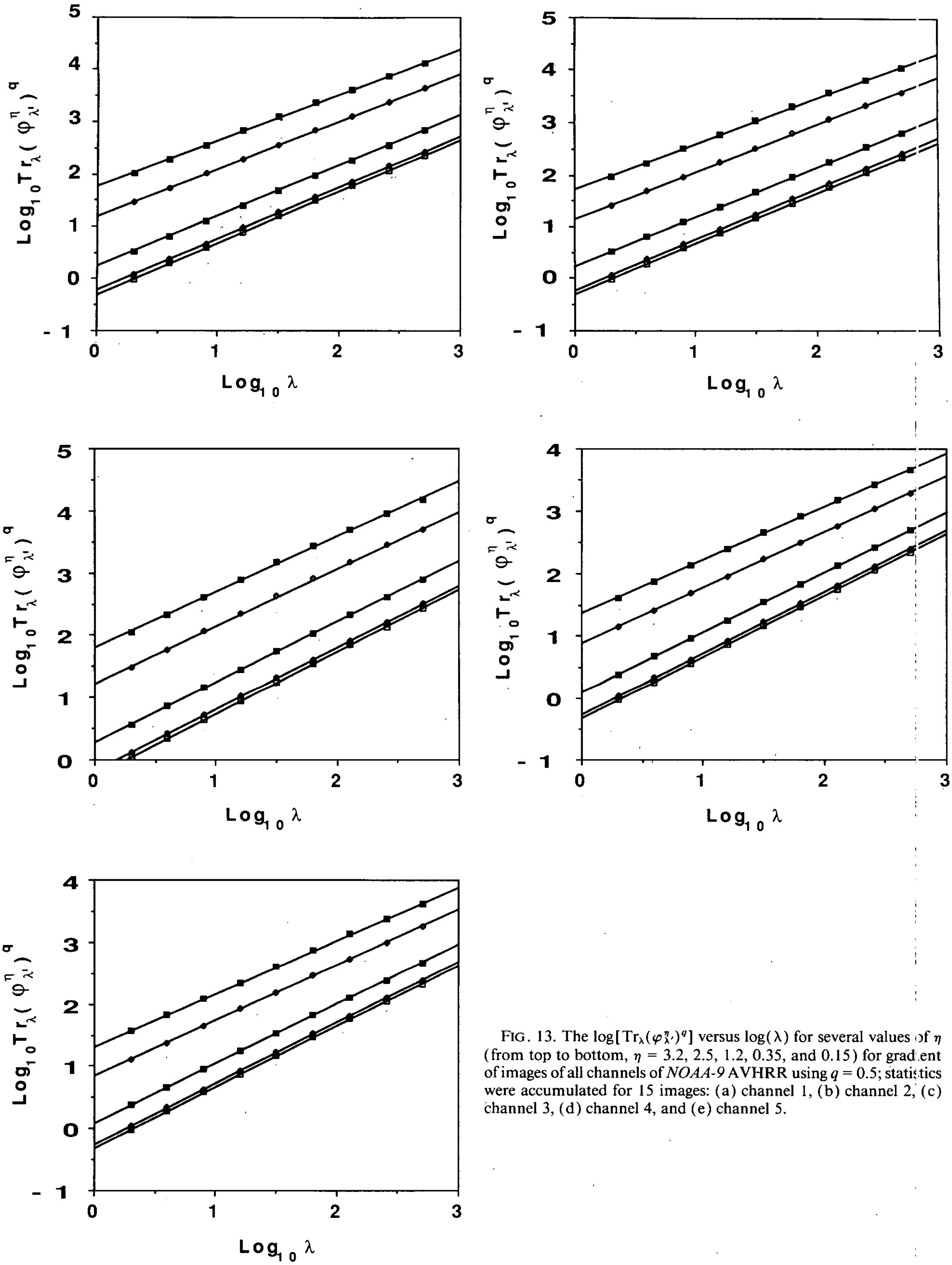

FIG. 13. The $\log[\mathrm{Tr}_\lambda(\varphi^{\eta}_{\lambda'})^q]$ versus $\log(\lambda)$ for several values of η (from top to bottom, $\eta = 3.2$, 2.5, 1.2, 0.35, and 0.15) for gradient of images of all channels of *NOAA-9* AVHRR using $q = 0.5$; statistics were accumulated for 15 images: (a) channel 1, (b) channel 2, (c) channel 3, (d) channel 4, and (e) channel 5.

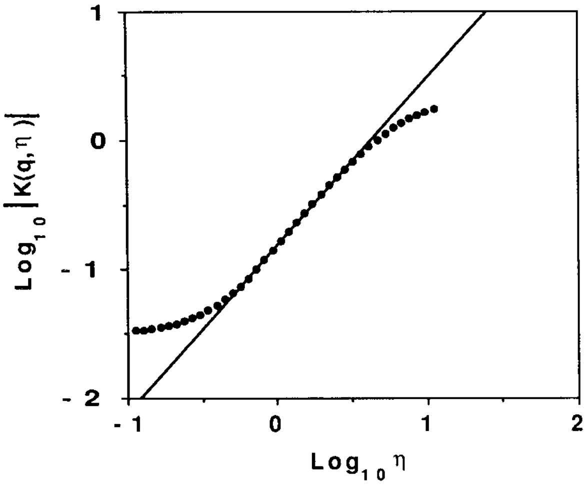

FIG. 14. The $\log[|K(q, \eta)|]$ versus $\log(\eta)$ for the gradient of an image taken by channel 5 of *NOAA-9*, a value of $q = 2.0$ is used and the straight line corresponds to the regression line from which $\alpha = 1.3$ and $C_1 = 0.1$ are deduced.

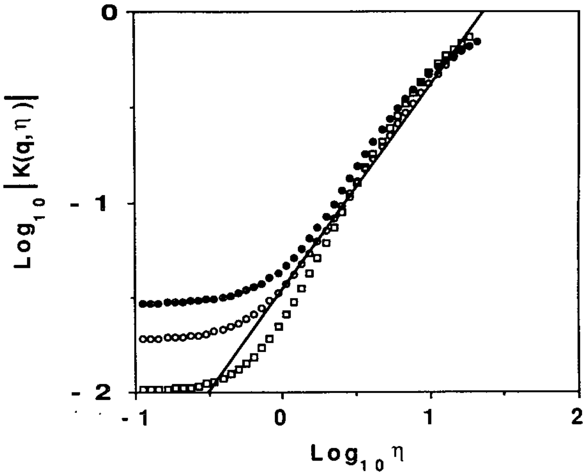

FIG. 16. The $\log[|K(q, \eta)|]$ versus $\log(\eta)$ with $q = 2.0$ for the gradient of all the images in the visible range. The straight line corresponds to $\alpha = 1.1$ and $C_1 = 0.1$. The empty squares are for Landsat, the empty circles for *NOAA-9* channel 1, and the filled circles for Meteosat visible channel.

is obtained for Landsat, $\alpha = 1.12$ and $C_1 = 0.12$ for Meteosat, and $\alpha = 1.07$ and $C_1 = 0.12$ for *NOAA-9* channel 1. The break in the linear behavior for low values of η should not be interpreted as a scaling break. In this range of η, the analysis is sensitive to extremely low values of the field being observed. Noise will overcome the signal from the expected linear behavior. Of course, different sensors will have different noise levels and this is why all the curves do not break at the same place. The next graph (Fig. 17) performs the same exercise for the thermal infrared sensors [channels 4 and 5 of *NOAA-9* and Meteosat Visible–Infrared Spin Scan Radiometer (VISSR) infrared channel]. The straight portions of the curves are nearly parallel and both channels of *NOAA-9* are almost on top of one another. The estimates for a are still close to one another ($\alpha = 1.21$ for Meteosat and $\alpha = 1.35$ for *NOAA-9*), and the estimates for C_1 are also compatible ($C_1 = 0.17$ for Meteosat and $C_1 = 0.09$ for *NOAA-9*). Table 2 summarizes all results for the different satelites and sensors.

All the observed values for α lie between 1 and 2. Since we always obtained $\alpha > 1$, the corresponding

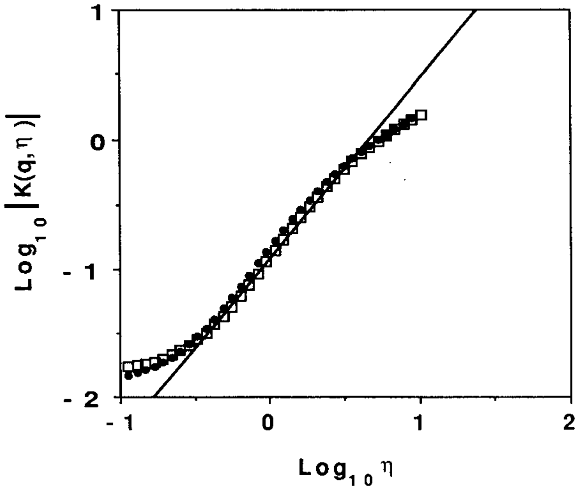

FIG. 15. The $\log[|K(q, \eta)|]$ versus $\log(\eta)$ for the Laplacian and the gradient of an image taken by the Landsat satellite. The filled circles are calculated using the Laplacian, and for the empty squares, the gradient was used. In both case $q = 2.0$. The straight line corresponds to $\alpha = 1.1$ and $C_1 = 0.1$.

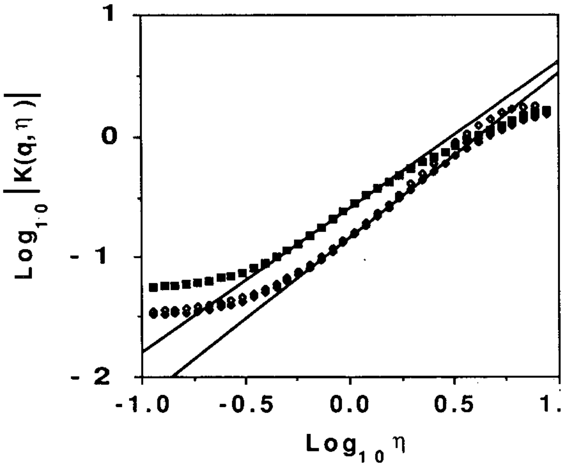

FIG. 17. The $\log[|K(q, \eta)|]$ versus $\log(\eta)$ with $q = 2.0$ for the gradient of images from the infra red sensors. The diamonds are for *NOAA-9* pictures (empty: channel 4; filled: channel 5) and the filled squares are for Meteosat pictures. The straight lines corresponds to linear regression fit on the linear part of the curves.

TABLE 2. The evaluated universal multifractal parameters for each group of pictures. The accuracy on the values of α is roughly estimated to be ±0.2, on C_1 it is ±0.1, and on H it is ±0.2.

Satellite	Sensor	Wavelength (μm)	Scaling range	α	C_1	H
NOAA-9	AVHRR channel 1	0.5–0.7	1–512 km	1.13	0.09	0.4
NOAA-9	AVHRR channel 2	0.7–1.0	1–512 km	1.10	0.09	0.4
NOAA-9	AVHRR channel 3	3.6–3.9	1–512 km	1.11	0.07	0.3
NOAA-9	AVHRR channel 4	10.4–11.1	1–512 km	1.35	0.10	0.5
NOAA-9	AVHRR channel 5	11.5–12.2	1–512 km	1.35	0.10	0.5
Meteosat	VIS	0.4–1.1	8–4000 km	1.35	0.10	0.3
Meteosat	IR	10.5–12.5	8–4000 km	1.21	0.09	0.4
Landsat	MSS	0.49–0.61	166 m–83 km	1.23	0.07	0.4

radiance fields will be unconditionally hard multifractal processes (section 2): that is, sufficiently high-order moments will diverge when the reflectivity field is averaged over a space of dimension D. The critical order for divergence is given by (2.11b); taking $D = 2$, it gives values of $q_D > 50$, which is sufficiently large to require enormous sample sizes for its observation. (The relevant value of D may be much smaller, in which case q_D will also be much smaller, and hence the divergence detectable. This is because research in progress indicates that the relevant D may be the order of fractional integration.)

There are many possible explanations for the spread in these values. First one has to remember that these universal parameters are well defined only for ensemble-average quantities, so that some statistical variation is certainly to be expected. For example, using numerical simulations with 25 independent one-dimensional samples with 1024 points each, Lavallée et al. (1991) estimated that α could be estimated to an accuracy of approximately ±0.1, which is a rough indication of the enormous sample sizes that are theoretically required (note that what is most fundamental is the range of scales and the number of independent realizations: here $\lambda = 256$ or 512 and 3–5 realizations were used). Second, different satellites have different problems. For example, Landsat was not designed for the observation of clouds, so that occasionally (~30% of the images in these cases) the detector was saturated by particularly bright cloud regions (with albedo greater than 0.45). Roughly the effect of this on the multifractal analysis is to cut off high-order singularities corresponding to the saturation level. Fortunately, our estimates of α and C_1 from the DTM technique mainly rely on the less extreme values (i.e., the low-order moments η, $q\eta \approx 1$) near the mean and should not be badly biased. Some Meteosat images were not completely over the ocean and it was possible to see landmasses under the clouds, so the analyzed albedo field is not purely due to clouds but in some part also to the land beneath them (which will presumably have different multifractal properties and exponents). Since at visible wavelengths the land has much lower radiance than clouds, this will primarily affect the very low η, $q\eta$ scaling and $K(q, \eta)$ estimates, again allowing reasonable C_1, α estimates from the DTM technique.

Selection bias was avoided as much as possible. All images in our largest set (*NOAA-9*) were taken with the sensor centered at 27.5°N, 70°W. This point is situated over the Atlantic Ocean, east of Florida. The 15 scenes were each taken at about 1400 ± 20 min EST during the month of February 1986 (the exact dates are 10–20, 22, 24, 25, and 27 February). The three Landsat images are part of a bigger (400 km × 400 km) picture, which itself was selected to have 90% cloud coverage, and the three Meteosat images are part of a sequence taken at 0.5-h intervals at the same location. So within each set, the images are not as completely independent as one would desire. Clearly in the future, massive systematic analyses must be undertaken.

Another problem that might have contributed to the spread of values for α is anisotropic scaling. Both the spectra and the DTM method as implemented here are entirely isotropic analysis techniques since the resolution of the fields is degraded isotropically (e.g., by using square boxes at all scales in the DTM method). As shown by Pflug et al. (1993), however, rotation and stratification of structures (due here to the Coriolis force) is important, hence more precise analyses should use generalized scale changes.

Recalling that C_1 characterizes the sparseness of the mean, whereas α characterizes the rate at which the sparseness varies as we go away from the mean, we expect C_1 to be more accurately estimated than α. This is indeed the case since for C_1, the range of values observed varies between 0.07 and 0.13. Such low values of C_1 are an indication that the conserved multifractal φ is not too sparse (a space-filling mean would have $C_1 = 0$). It also explains the relative success of monofractal analyses (e.g., Lovejoy 1982), since near the mean, the parameter H will provide a reasonable approximation to the scaling. Since α is fairly large (far from the monofractal value of zero), as one moves away from the mean value, the monofractal approximation rapidly becomes poorer. For more discussion of monofractal cloud analyses, their limitations, and their biases (due to multifractal effects), see Lovejoy and Schertzer (1991), especially the appendixes.

c. The horizontal scaling of rain reflectivities

The relative success of satellite-based rainfall-estimation schemes (such as RAINSAT; Bellon et al. 1980)—which use both radar reflectivities and raingage measurements for ground truth—proves that there is indeed an intimate relation between visible and infrared radiances, rain, and radar reflectivities of rain. Therefore, our attention is turned from the radiances to datasets more closely related to rainfall. The first such dataset studied was obtained using a scanning radar situated in Montreal. This radar provides information for 24 elevation angles at a wavelength of 10 cm with a pulse repetition rate of 300 Hz and a downrange resolution of 75 m. Scans were analyzed during a convective storm over Montreal that took place at 2200 EST 1 May 1992. From these scans, 256 × 256 square section images were analyzed (avoiding the center and the outer limit, which were biased due to ground echo and the curvature of the earth). In order to avoid ground-clutter contamination, the smallest elevation angles were not used. The first analysis done was the isotropic power spectrum, which is shown on Fig. 18. Scaling is observed on the range of 75 m to 10 km. From a linear regression, the (negative) spectral slope is deduced to be $\beta \approx 1.45$. Figure 19, where $\log[\mathrm{Tr}_\lambda(\varphi^{\eta}_{\lambda'})^q]$ versus $\log\lambda$ is shown for various η, confirms that there is scaling over the entire range studied. The $\log[|K(q, \eta)|]$ versus $\log\eta$ curve, calculated from the previous graph, is shown in Fig. 20. In this case, $\alpha \approx 1.4$ and $C_1 \approx 0.12$.

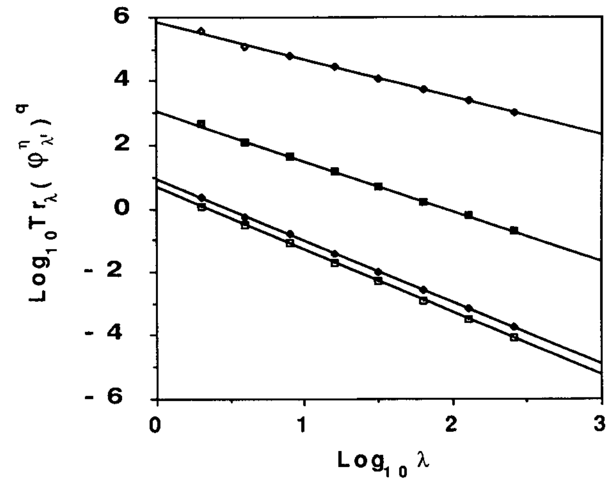

FIG. 19. The $\log[\mathrm{Tr}_\lambda(\varphi^{\eta}_{\lambda'})^q]$ versus $\log(\lambda)$ for several values of η (from top to bottom, $\eta = 2.7$, 1.61, 0.4, 0.2) using $q = 2.0$ for the gradient of radar PPIs.

d. The vertical scaling of rain reflectivities

In the previous section, an estimate of the universal parameters was obtained for the horizontal radar reflectivity field. In order to look at the vertical structure, our attention was turned to another dataset. The data studied were obtained using a vertically pointing (3-cm wavelength) radar with a pulse repetition rate of 0.4 Hz. A dataset lasting for 5 h 41 min 20 s (8192 consecutive pulses), with near range of the 171-m altitude above the radar and far range of 6958 m above (in 325 equally spaced bins, 21.4-m pulse length) was

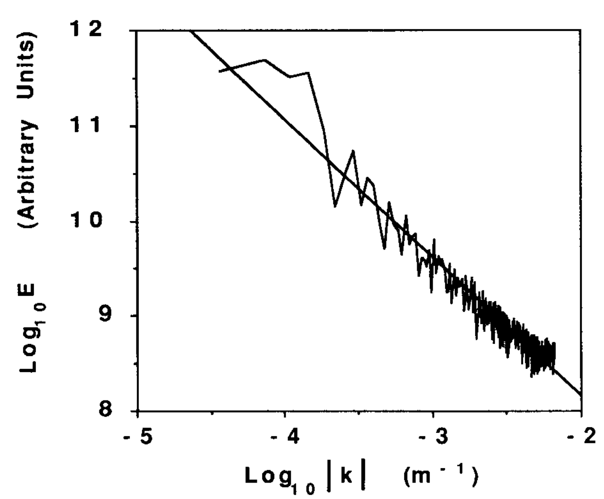

FIG. 18. Isotropic power spectrum for radar PPIs. A line of slope −1.45 is included so that the scaling behavior is more apparent.

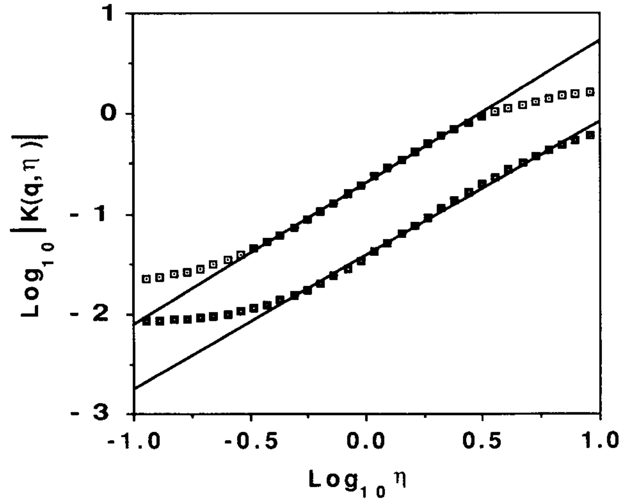

FIG. 20. The $\log[|K(q, \eta)|]$ versus $\log(\eta)$ with $q = 2.0$ (top curve) and $q = 0.5$ (bottom curve) for radar PPIs. The straight lines corresponds to $\alpha = 1.4$ and $C_1 = 0.12$.

analyzed. The vertical structure of rain reflectivities is quite different from the horizontal structure due to the strong stratification caused by gravity (Lovejoy et al. 1987).

The meteorological situation involved stratiform rain ahead of the warm sector of a low. The surface temperature varied between 8° and 10°C during the storm. There was a bright band (i.e., melting snow and ice) between the 1.5- and 2.5-km altitudes. A small portion of the raw data is shown in Fig. 21. When the horizontal cloud radiances were analyzed, the (usual) isotropic energy spectrum obtained by integrating the Fourier square moduli over angles in Fourier space (and then estimating the ensemble average by averaging over the available data) were immediately calculated. This was natural since in the horizontal plane, the anisotropy was not too pronounced. Here the situation is quite different since, a priori, the vertical and temporal characteristics of rain are very different, the (k, ω) [Fourier space, corresponding to (z, t) real space] will be quite anisotropic—strongly stratified in the z direction (as may be seen in Fig. 22). The proper framework for analyzing this anisotropy is GSI, and the related space–time transformations are discussed more in detail in section 5. This section is limited to more straightforward analyses. First, lines of constant Fourier amplitudes are calculated in the two-dimensional (k, ω) space (Fig. 22). As expected, we roughly obtain ellipses whose stratification is opposite that of the real space (z, t) stratification (and increases with increasing k). The slight overall rotation corresponds to a constant advection velocity. This differential stratification corresponds to the fact that (one-dimensional) temporal and (one-dimensional) spatial spectra will have different spectral exponents (β_t, β_v). Indeed, the one-dimensional vertical spectrum for the region below the bright band (Fig. 23, averaged over all the pulses in time) shows $\beta_v \sim 1.4$, whereas the corresponding temporal spectrum (Fig. 24) average over different portions corresponding to different ranges of altitudes yields $\beta_t \sim 1.2$. The break in the vertical spectrum occurs at scales of approximately 100 m and roughly coincides with the horizontal scale of averaging—the pulse width in the horizontal was 100 m at the 3-km distance. Figure 22, shows the "spheroscale," which is the scale over which the (near) elliptical contours become (near) circles, indicating approximate isotropy at the corresponding scale (approximately 1 km here). The existence of a bright band limited these analyses in Fig. 23 to a range of only a factor 64. This vertical scaling confirms that already reported using an entirely different method: functional box counting [Lovejoy et al. (1987) found that reflectivities of ten stratiform and ten cumuloform storms were fairly accurately scaling over the range 1–8 km].

For each pulse, trace-moment statistics of 64 levels

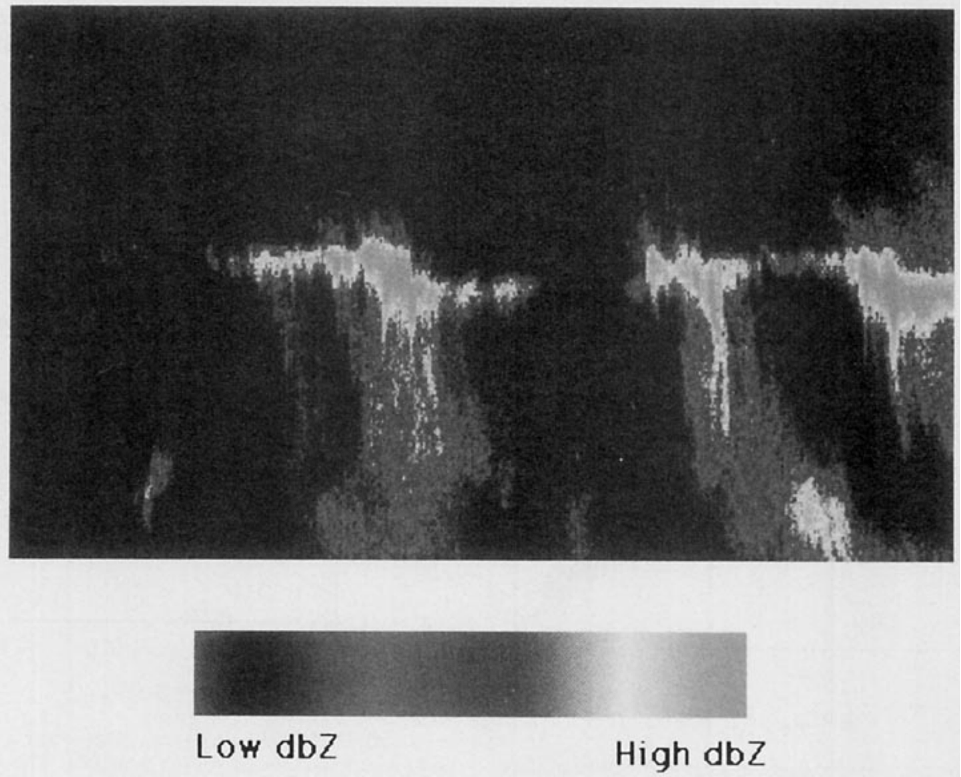

FIG. 21. A portion of the raw data for the vertically pointing radar reflectivities. A 1024 time steps × 318 vertical bins section is shown. The gray scale is proportional to the dbZ value.

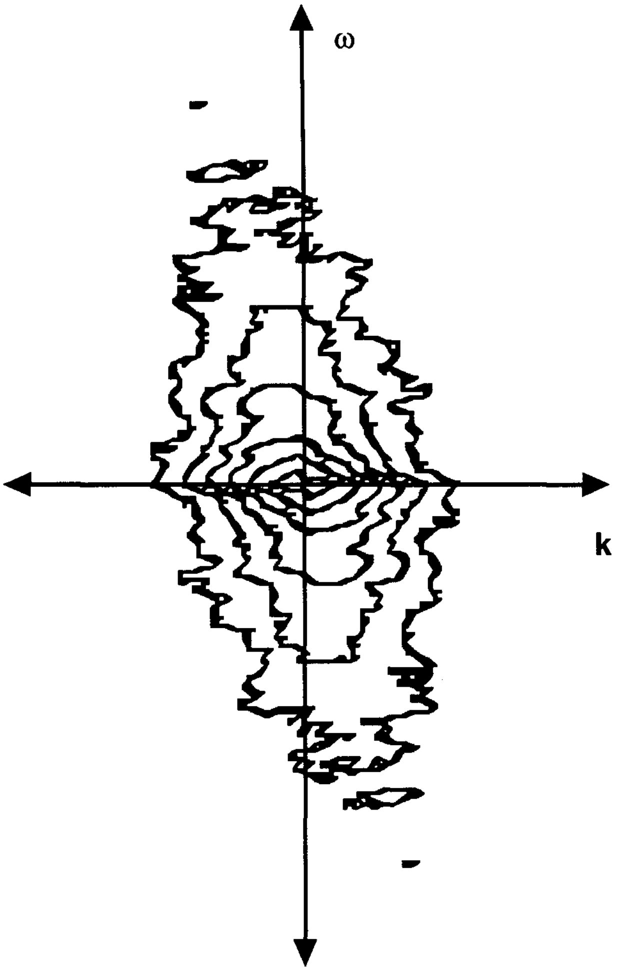

FIG. 22. Two-dimensional power spectrum isolines for radar reflectivities. It can be seen that the isolines are highly elongated in the temporal frequency direction for high frequencies and in the spatial direction for low frequencies.

below brightband levels were calculated, as well as the statistics over the 8192 pulses. Figure 25 shows the log of the trace moment of order $q = 2$ against the log of the scale ratio λ for different values of the exponent η. It can be seen that we obtained scaling over nearly two orders of magnitude in λ (corresponding to the high-frequency scaling in Fig. 24). Figure 26 shows $\log|K(q, \eta)|$ versus $\log\eta$ for $q = 0.5$ and $q = 2.0$, from which we deduce $\alpha \approx 1.35$ and $C_1 \approx 0.1$.

e. The horizontal structure of global raingage data

The next rain dataset examined was the daily rainfall accumulations observed by raingages at synoptic weather stations covering the earth for 1983 (Fig. 27). This dataset was archived at the National Meteorological Center (NMC) of the National Oceanic and Atmospheric Administration (NOAA).

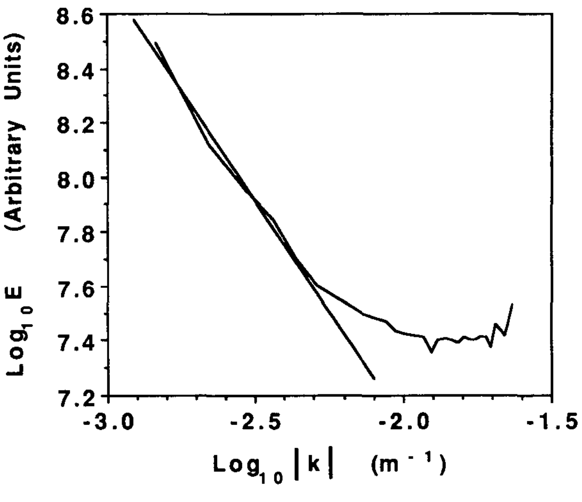

FIG. 23. Power spectrum for the radar reflectivities against elevation. From the slope of the regression line, $\beta = 1.4$.

The obvious difficulty with this in situ dataset is that it is far from uniform; the stations themselves have a fractal dimension of approximately 1.75 (Lovejoy et al. 1986), indicating that "holes" do indeed occur at all scales (at least from global scales down to 150 km). In fact, as discussed in Tessier et al. (1992b), it is best to treat the density of stations as a multifractal measure (rather than the stations themselves as a fractal set) and then to statistically correct for the multifractal nature of the network.

In what follows, the correction method given in Tessier et al. (1992b) is summarized. Consider that the measuring stations have a multifractal density ρ_λ when measured at resolution λ. This was found to be a reasonable approximation to the density field over the

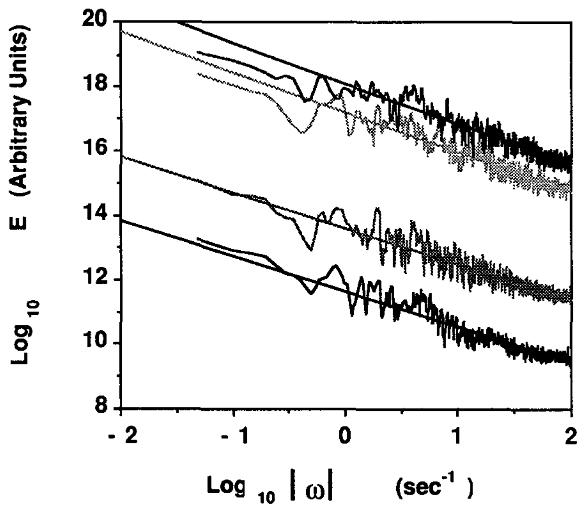

FIG. 24. Power spectrum for the radar reflectivities against time. From the slope of the regression line, $\beta = 1.2$ is deduced.

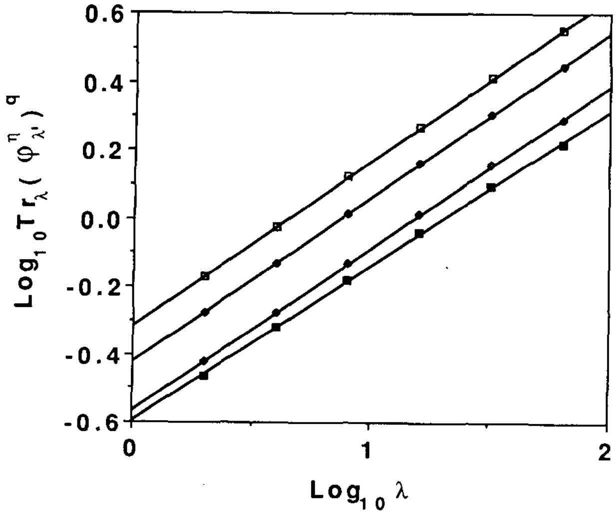

FIG. 25. The $\log[\mathrm{Tr}_\lambda(\varphi^\eta_{\lambda'})^q]$ versus $\log(\lambda)$ for several values of η (from top to bottom, $\eta = 1.2, 0.7, 0.3$ and 0.1) for radar reflectivities against elevation and statistics accumulated in time. Here $q = 0.5$ is used.

range of approximately 5.0×10^4 to 1.5×10^2 km (the lower limit arises because there were only about 8000 stations, which is finite). We now indicate how the DTM method can be applied to the sparse data and provide a simple and elegant method for statistically removing the associated measurement bias.

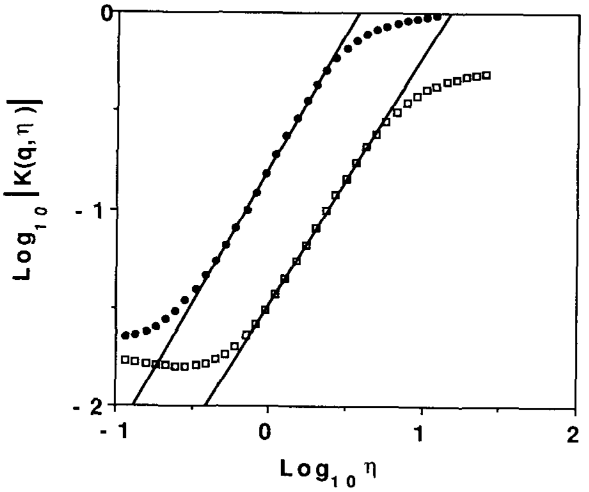

FIG. 26. The $\log[|K(q, \eta)|]$ versus $\log(\eta)$ for the radar reflectivities against elevation and statistics accumulated in time. The empty squares are for $q = 0.5$ and the filled circles are for $q = 2.0$. From the regression lines, $\alpha = 1.35$ and $C_1 = 0.1$ are deduced.

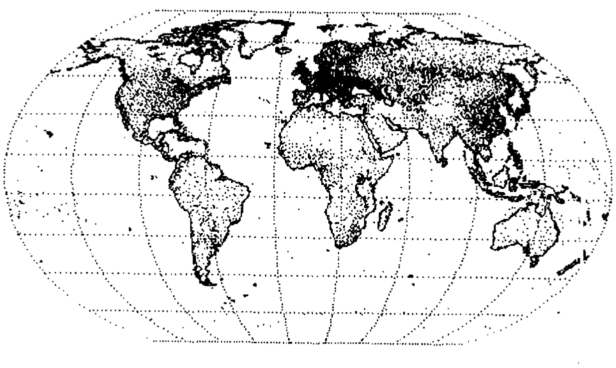

FIG. 27. Position of the stations reporting daily rainfall accumulations in 1983 that have been used in our analysis. The continent layouts have also been plotted for reference.

Consider the sum over the ith grid-box (or circle) scale λ ($B_{\lambda,i}$) of the raw rainfall accumulations raised to a power η : $\sum_{B_{\lambda_i}} R^\eta_{\lambda'}$. The subscript λ' is used in the same sense as (3.1) for the DTM, it is the spatial scale associated with the (daily) accumulation period (averaging in time will smooth in space at a scale determined by the corresponding space–time transformation; see section 5). This sum is an estimate of the product $\rho_\lambda R^\eta_{\lambda'}$ integrated over the ith ball:

$$\sum_{B_{\lambda,1i}} R^\eta_{\lambda',i} \approx \int_{B_{\lambda,i}} \rho_\lambda R^\eta_{\lambda'} d^D x$$

$$\approx \rho_\lambda \int_{B_{\lambda,i}} R^\eta_{\lambda'} d^D x \approx \rho_\lambda \Pi^{(\eta)}_{\lambda'}(B_{\lambda,i}), \quad (4.2)$$

where $\Pi^{(\eta)}_{\lambda'}(B_{\lambda,i})$ is the η flux corresponding to R in the ith ball. The sum is over all the j stations in the ith ball. Since ρ_λ is constant over $B_{\lambda,i}$ and here $D = 2$, the sets $B_{\lambda,i}$ are two-dimensional boxes or circles. The following double trace moment is now defined:

$$\langle \sum_i (\sum_{j \in B_{\lambda,i}} R^\eta_{\lambda',j})^q \rangle = \lambda^{K_{\mathrm{meas}}(q,\eta)-(q-1)D}. \quad (4.3)$$

This double trace moment can be estimated as

$$\langle \sum_i [\rho_\lambda \Pi^{(\eta)}_{\lambda'}(B_{\lambda,i})]^q \rangle \approx \langle \rho^q_\lambda \rangle \langle \Pi^{(\eta)q}_{\lambda'}(B_\lambda) \rangle \quad (4.4)$$

$$\approx \lambda^{K_\rho(q,1)} \lambda^{K_R(q,\eta)-(q-1)D}, \quad (4.5)$$

where we have assumed statistical independence of the network and the rain field (ρ_λ and R_λ). Thus,

$$K_{\mathrm{meas}}(q, \eta) = K_R(q, \eta) + K_\rho(q, 1) \quad (4.6)$$

is obtained. The measured multiple-scaling function $K_{\mathrm{meas}}(q, \eta)$ can readily be used to determine $K_R(q, \eta)$ by exploiting the fact that $K_R(q, 0) = 0$, hence:

$$K_{\mathrm{meas}}(q, 0) = K_\rho(q, 1) \quad (4.7)$$

$$K_R(q, \eta) = K_{\mathrm{meas}}(q, \eta) - K_{\mathrm{meas}}(q, 0). \quad (4.8)$$

From such an analysis, the (network corrected) values $\alpha = 1.34 \pm 0.09$ and $C_1 = 0.16 \pm 0.03$ are obtained, as may be seen in Fig. 28 where $\log|K(q, \eta)|$ versus $\log\eta$ has been plotted for $q = 0.5, 1.5,$ and 2.0. These values are, in fact, in excellent agreement with what

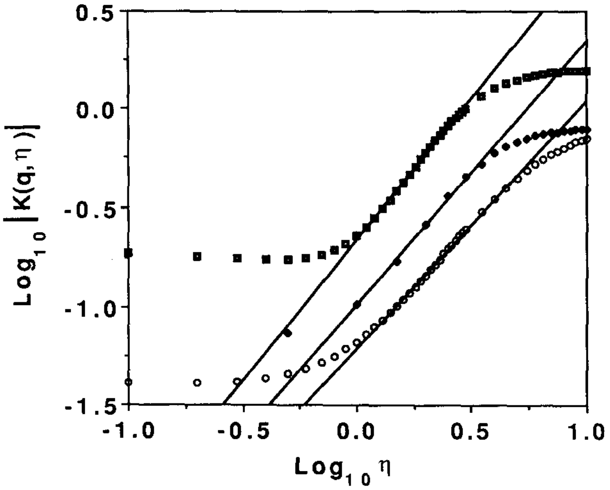

FIG. 28. The $\log[|K(q, \eta)|]$ versus $\log(\eta)$ for daily rainfall accumulations on a global network after the needed corrections explained in the text. From top to bottom, curves for $q = 2.0$, 1.5, and 0.5 are shown. The regression lines on the different curves give a value of $\alpha = 1.34 \pm 0.09$ and $C_1 = 0.16 \pm 0.03$.

was obtained from radar observations. To understand the relationship between radar reflectivities and rain rates, note that the simplest statistical relation between the two that respects scaling is a power law, that is, $Z = bR^a$. Indeed, such power laws are frequently invoked in rain (e.g., the well-known semiempirical Marshall–Palmer law has exponent $a = 1.6$). Writing $Z = \lambda^{\gamma_z}$ and $R = \lambda^{\gamma_R}$, this is equivalent to the linear transformation of singularities: $\gamma_z = a\gamma_R$, where γ_z is the singularity in Z, and γ_R is the corresponding singularity in R. It has already been seen [(3.6) with $\eta = a$] that under such transformations, $\alpha \rightarrow \alpha$, and $C_1 \rightarrow C_1 a^\alpha$. In fact, $\alpha \sim 1.4$ for both datasets. We also find $C_{1Z} = a^{-\alpha} C_{1R}$, which is roughly satisfied with the Marshall–Palmer value $a \sim 1.6$, $\alpha \sim 1.5$, $C_{1Z} \sim 0.3$, and $C_{1R} \sim 0.2$. The agreement between the values of α is particularly significant considering the apparently very different natures of the datasets involved. The consistency of the C_1 estimates is less significant since C_{1Z} is for the vertical reflectivities, whereas C_{1R} is for the horizontal rain. The two are expected to differ not only because of the Z-R relation but also because of the horizontal–vertical anisotropy.

5. The temporal structure of rain

a. Comparing spatial and temporal scaling

The spatial variability of various fields related to the distribution of water in the atmosphere has been discussed, our attention is now turned to the problem of temporal variability. There are many reasons for studying this variability. In many applications, knowledge of how the rainfall intensity at a point varies with time is an important issue all by itself. More fundamentally, the relation between the spatial and the temporal variability of turbulent fields is an outstanding theoretical problem. An understanding of the space–time relation is necessary in estimating water budgets, as well as in making predictions (as is already recognized by various data-assimilation schemes). Probably the most cited and widely used method of relating time and space is "Taylor's hypothesis of frozen turbulence" (Taylor 1938), which basically states that temporal t and spatial averages l are related by a constant velocity v in a relation of the form $l = vt$. Although this hypothesis has been widely used since the 1930s in both atmospheric and laboratory turbulence, Zawadzki (1973) was the first to give it a (limited) test in rain using radar data. Although turbulence in the atmosphere is not "frozen," a statistical version of the hypothesis might still apply: that is, the statistical properties in space and time are the same (if appropriately rescaled using a velocity parameter). If this statistical version held, then rain would be isotropic in space–time. Recently, Lovejoy and Schertzer (1991) have analyzed lidar data of rain, indicating that an anisotropic generalization of Taylor's hypothesis (discussed below) based on a turbulent (i.e., scale dependent) velocity is more appropriate than assuming frozen turbulence and space–time isotropy. Below, no specific relation between time and space is presupposed: the universal parameters characteristic of the process in time and in space are determined separately. This will provide some of the information needed to determine the space–time transformation operator, an issue that will be fully developed elsewhere.

The same fixed vertical radar data discussed in section 4c is used, and it has already been indicated that the temporal scaling is well respected (Fig. 24). We

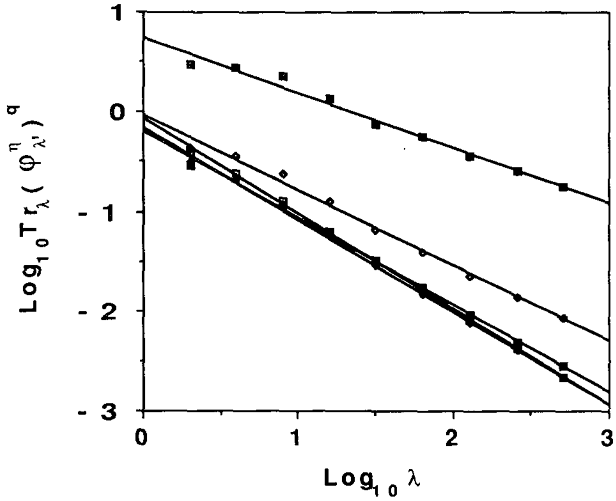

FIG. 29. The $\log[\mathrm{Tr}_\lambda(\varphi^\eta_{\lambda'})^q]$ versus $\log(\lambda)$ for several values of η (from top to bottom, $\eta = 2.1$, 1.1, 0.6, 0.4, and 0.2) for the gradient of radar reflectivities against time and statistics accumulated for different elevations. Here $q = 2.0$ was used.

now discuss applying DTM analysis (on the modulus of the gradient) of a section of duration 8192 × 2.5 s (i.e., 5 h 41 min 20 s). We accumulated statistics for the 256 levels closest to the ground. Figure 29 shows the log of the trace moment of order q against the log of the scale ratio λ for different values of the exponent η. Again, it can be seen that scaling is obtained over the range of three orders of magnitude in λ (60–20 000 s). Figure 30 shows $\log|K(q, \eta)|$ versus $\log\eta$ for $q = 0.5$ and $q = 2.0$, from which $\alpha \approx 0.7 \pm 0.2$ and $C_1 \approx 0.5 \pm 0.2$ are deduced. The spectral slope for the radar scans was already found to be $\beta \approx 1.2$ (Fig. 24), which gives (using the above values of α and C_1) a value of $H \approx 0.4$ [this is close to the value $H \approx 0.5$ found in Lovejoy (1981) for isolated rainstorms evolving in time estimated using probability distributions; see also Lovejoy and Mandelbrot (1985)].

These temporal statistics can now be compared with those obtained for the global dataset discussed in section 4d. Figure 31 shows the results of the DTM for daily rainfall where $\log|K(q, \eta)|$ versus $\log\eta$ is plotted for $q = 0.5$ and $q = 1.5$. The period of time studied was 64 days, and the statistics were accumulated for 4000 stations (only those stations with continuous data for 64 consecutive days were used). The values obtained were $\alpha \sim 0.55$, $C_1 \sim 0.6$. Details of the analysis are reported elsewhere (Tessier et al. 1992b). Other reports also agree with these estimates: Hubert et al. (1992) used time series of gauge rainfall for Reunion Island obtaining $\alpha = 0.5$ and $C_1 = 0.2$. Indeed, in the same paper, these parameters are used to (correctly) reproduce the behavior of extreme rainfall events in many locations around the world. Ladoy et al. (1992) analyzed a 30-yr record of daily rainfall accumulation over Nîmes, France, and obtained $\alpha \approx 0.4$ and $C_1 \approx 0.6$ (their $\log K$ versus $\log\eta$ curve is reproduced in Fig. 32). Finally, note that also for the same dataset (Nîmes) Ladoy et al. (1991) obtained $\beta \approx 0.3$, which gives $H \sim 0$. Hence, (unlike the radar scans) the actual field for the rainfall accumulations was analyzed here—we expect no complications due to fractional integration. As a last comment, we should note that Seed (1989), using a rather different technique (the "probability distribution multiple scaling" technique) on radar reflectivities of four separate convective storms in

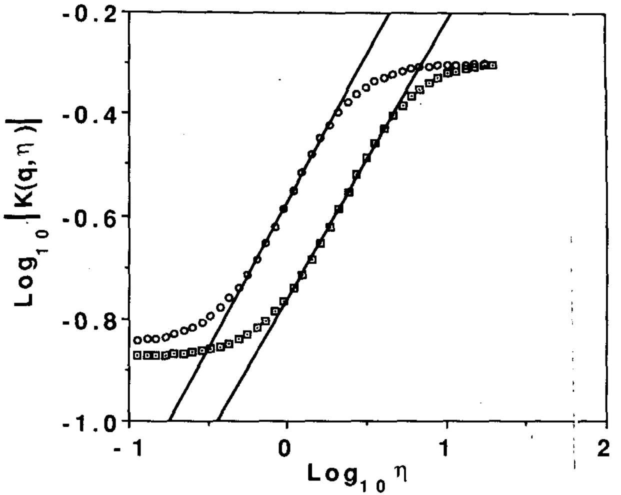

FIG. 31. The $\log[|K(q, \eta)|]$ versus $\log(\eta)$ for daily rainfall accumulations on a global network were we have considered the time series for each stations and accumulated statistics for 4000 stations. The regression line gives a value of $\alpha = 0.55$ and $C_1 = 0.6$.

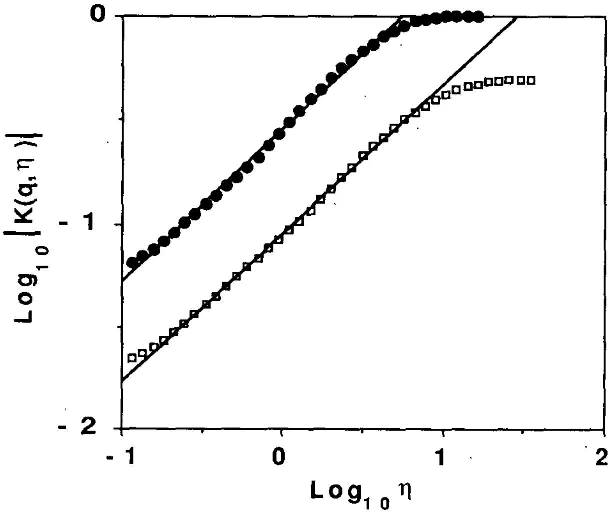

FIG. 30. The $\log[|K(q, \eta)|]$ versus $\log(\eta)$ for the gradient of the radar reflectivities against time and statistics accumulated for different elevation. The empty squares are for $q = 0.5$ and the filled circles are for $q = 2.0$. From the regression lines, it is deduced that $\alpha = 0.7$ and $C_1 = 0.3$.

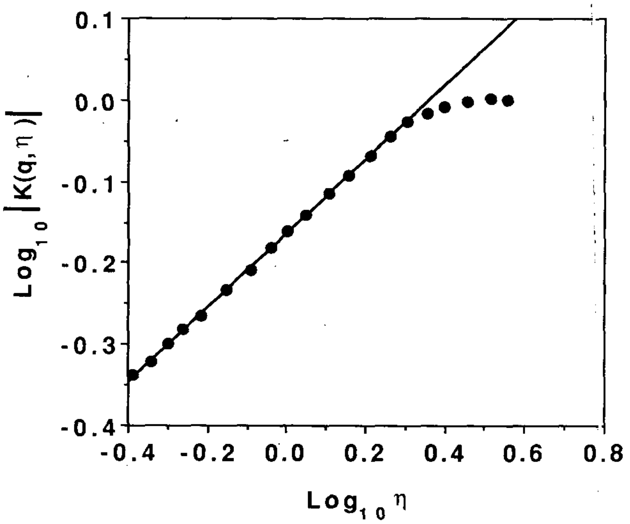

FIG. 32. The $\log[|K(q, \eta)|]$ versus $\log(\eta)$ for daily rainfall accumulations recorded in Nimes, France, for a period of 30 years. The regression line gives a value of $\alpha = 0.5$ and $C_1 = 0.6$. (Reproduced from Ladoy et al. 1992.)

Montreal, found α in the range 0.3–0.6 and C_1 in the range 0.6–1.0. His results, however, used poorly conditioned nonlinear regressions leading to low accuracy in the estimates. Although he averaged in space, he pooled statistics into histograms involving many (~ 144) consecutive 5-min PPIs. Given the difference in α values between time and space found here, his results can be better understood, since when using histograms the lower value of α will dominate because it is the α' that is important [see (2.9)]; his estimates are in fact close to the more accurately estimated temporal parameters found here.

b. The theoretical framework for space–time transformations: Generalized scale invariance

If, as argued in this paper, the scaling of cloud radiance, rain reflectivities, and other atmospheric fields continues from small scales right through the mesoscale (there is no mesoscale gap), then no large-scale forcing velocity can be appealed to in order to transform from space to time, and turbulent velocities must be used instead. At scale λ, they will have amplitudes $v_\lambda \approx \langle \epsilon_\lambda^{1/3} \rangle \lambda^{-1/3}$, where λ^{-1} is the scale of the eddy, ϵ_λ is the energy flux through the eddy to smaller scales [(2.2) with $l = \lambda^{-1}$]. Although $\langle \epsilon_\lambda \rangle$ is scale independent, $\langle \epsilon_\lambda^{1/3} \rangle \approx \lambda^{K(1/3)}$. Since $K(1/3)$ is small compared with $1/3$, it will be written as δ. Rather than being scale independent, the space–time transformation will thus have a scale-dependent velocity[11] $v_\lambda \approx \lambda^{-H}$ with $H \approx 1/3 + \delta$. The two geophysically relevant Taylor's hypotheses therefore correspond to $H = 0$ or $H = 1/3 + \delta$, depending on the existence (or not) of the "gap."

The theoretical arguments mentioned above make it clear that the turbulent velocity is likely to be relevant for space–time transformations. The space–time transformation inferred from the turbulent value of H ($\approx 1/3$) can be easily expressed in the formalism of generalized scale invariance. Considering (x, y, t) space, the space–time transformation can be simply expressed by statistical invariance with respect to the following transformation: $x \rightarrow x/\lambda$, $y \rightarrow y/\lambda$, $t \rightarrow t/\lambda^{1-H}$, or using the notation $r = (x, y, t)$, $r_\lambda = \mathbf{T}_\lambda r_1$ with $\mathbf{T}_\lambda = \lambda^{-\mathbf{G}}$ and

$$\mathbf{G} = \begin{bmatrix} 1 & 0 & 0 \\ 0 & 1 & 0 \\ 0 & 0 & 1-H \end{bmatrix}. \qquad (5.1)$$

The matrix **G** could also have off-diagonal elements to account for stratification and rotation. The elements of this matrix **G** could be identified using the Monte Carlo rotating-ellipse technique. Pflug et al. (1992) successfully used this technique to classify satellite cloud images according to the amount of stratification and rotation present. This formalism, when applied to the space–time problem in rain, is expected to be quite complex since α for the velocity field in the atmosphere is approximately 1.5 (Schmitt et al. 1992c), and α was found to be different in time and space for the rain field.

c. Discussion

In our analyses, $\alpha \approx 0.6 \pm 0.2$ is obtained for all the time series of fields related to rainfall that have been analyzed. In spatial analysis, radar scans and daily rainfall accumulations both give $\alpha \approx 1.4 \pm 0.1$. The agreement on the values of this fundamental parameter coming from disparate types and sources of data gives us considerable confidence in these values, although the theoretical reason why agreement should be obtained does not stand on completely firm ground. It is interesting to compare these results to those obtained for cloud radiances. If we take the mean of all the visible and near-infrared images, we get $\alpha \approx 1.15 \pm 0.2$. If we take the mean of all the thermal IR images, we get $\alpha = 1.3 \pm 0.2$, which are both (to within statistical uncertainty) close to the $\alpha = 1.4$ value, especially if all the poorly understood effects that could bias our estimates of α discussed in section 4a are considered. In this case, there is less a priori reason to expect the existence of simple statistical relation between rain and radiance singularities, although if the values of α were the same, a fairly simple relationship might indeed exist.

The finding that the values of α for spatial and temporal processes belong to qualitatively different classes of probability distribution (unconditionally hard, $\alpha > 1$, conditionally soft, $\alpha < 1$; see section 2c) has profound consequences because it means that qualitatively different multifractal behavior will be observed in space and in time. Since $\alpha < 1$, there will be a maximum order of singularity $= C_1(1-\alpha)^{-1} \approx 1.2$ in time [this could explain the statistics of extreme rain events (see Hubert et al. 1992)], whereas in space, γ is unbounded [actually in both cases hard multifractal processes may be obtained, since even in time $C_1(\alpha - 1) > 1$ implies a finite q_D for $D \leqslant 1.2$. The multifractals in time are classified as being conditionally soft and those in space as being unconditionally hard. This distinction may also have consequences for the interpolation and extrapolation problem (multifractal objective analysis and multifractal forecasting).

6. Isotropic (self-similar) simulations of rainfall

This section indicates briefly how to exploit the universality (and the measured H, C_1, α parameters) to perform multifractal simulations. The first multifractal models of this type were discussed in Schertzer and Lovejoy (1987), and Wilson et al. (1991). The latter give a comprehensive discussion including many prac-

---

[11] Each moment of the rain field will require a different δ. For simplicity, this complication is ignored here.

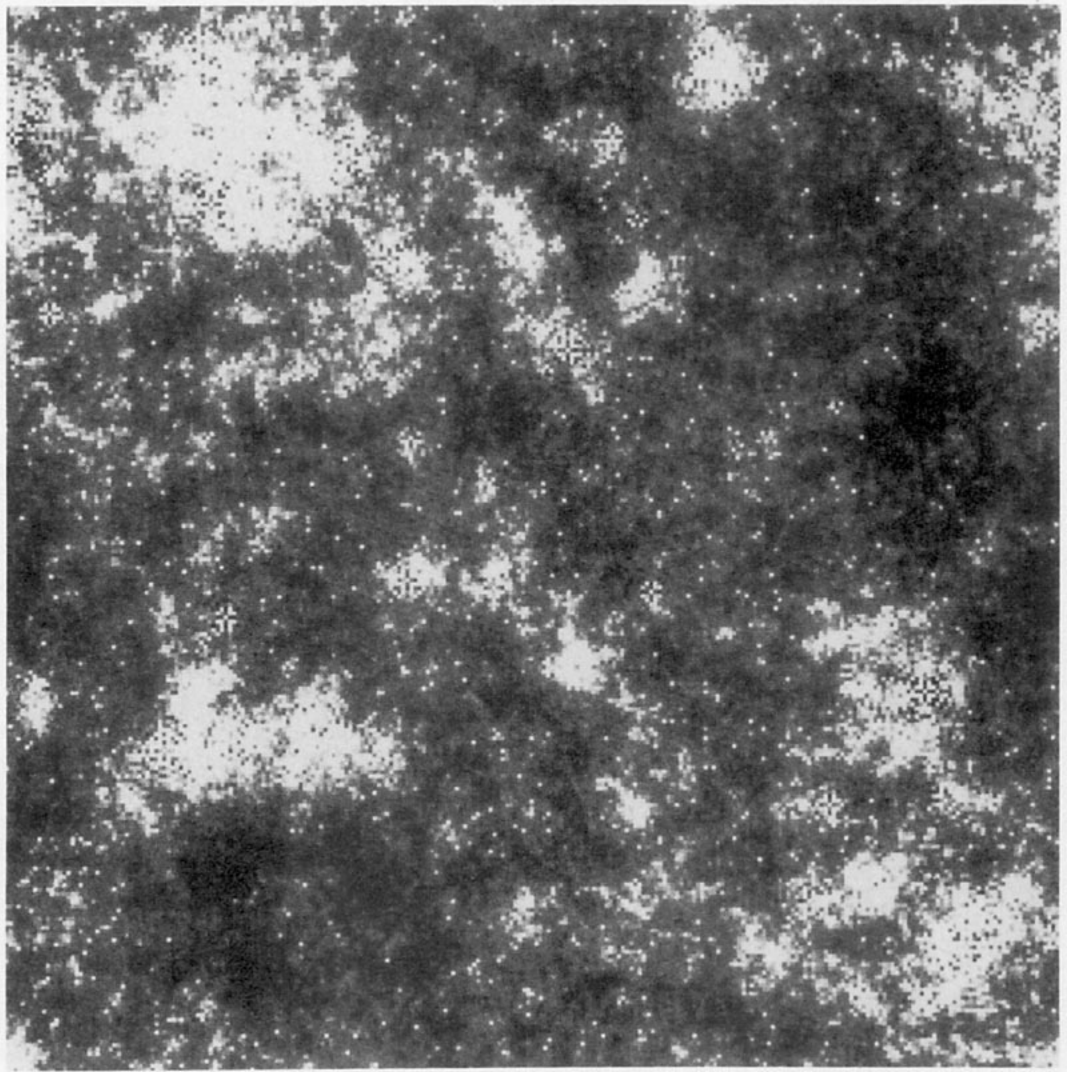

FIG. 33. Two-dimensional simulation using $\alpha = 1.35$, $C_1 = 0.1$, and $H = 0.3$. The values of the parameters are close to what has been estimated for cloud-radiance pictures in the visible frequencies range.

tical (numerical) details. In particular, Wilson et al. describe the numerical simulation of clouds and topography, including how to iteratively "zoom" in, calculating details to arbitrary resolution in selected regions. Although these details will not be repeated here, enough information has been given in the previous sections to understand how they work. First, for a conserved (stationary) multifractal process φ_λ we define the generator $\Gamma_\lambda = \log\varphi_\lambda$. To yield a multifractal φ_λ, it must be exactly a $1/f$ noise, that is, its generalized spectrum is $E(k) \approx k^{-1}$ (this is necessary to ensure the multiple scaling of the moments of φ_λ). To produce such a generator, we start with a stationary Gaussian or Levy "subgenerator." The subgenerator is a noise consisting of independent random variables with either Gaussian ($\alpha = 2$) or extremal Levy distributions (characterized by the Levy index α), whose amplitude (e.g., variance in the Gaussian case) is determined by C_1. The subgenerator is then fractionally integrated (power-law filtered in Fourier space) to give a k^{-1} spectrum. This generator is then exponentiated to give the conserved φ_λ, which will thus depend on both C_1 and α. Finally, to obtain a nonconserved process with spectral slope β, the result is fractionally integrated by multiplying the Fourier transform by k^{-H}, where H is given in (3.8). The entire process involves two fractional integrations and hence four FFTs. The 512 × 512 fields can easily be modeled on personal computers (they take about 3 min on a Macintosh II), and 256 × 256 × 256 fields (e.g., space–time simulations of dynamically evolving multifractal clouds) have been produced on a Cray 2 (Brenier 1990; Brenier et al. 1990). (Such cloud simulations have been turned into a video called "multifractal dynamics.")

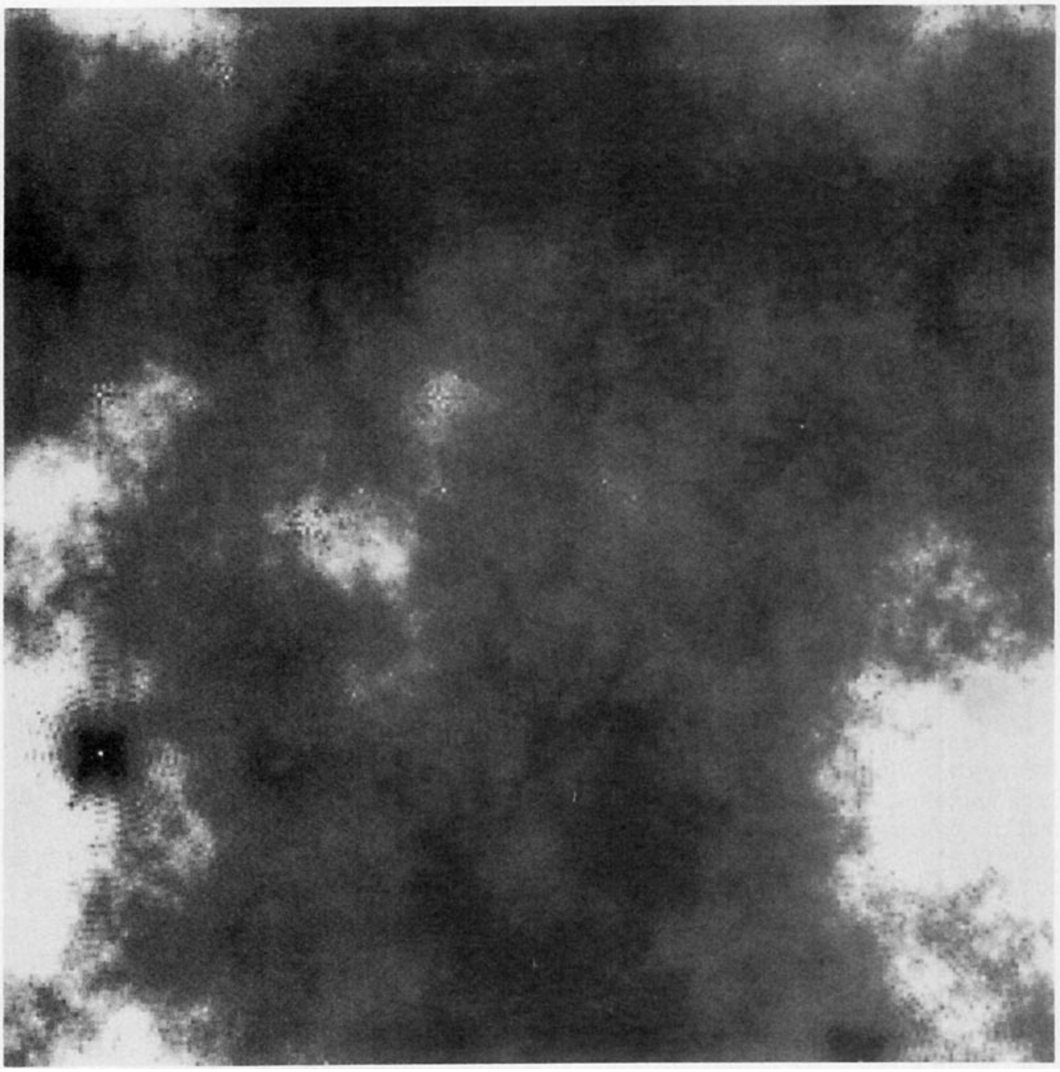

FIG. 34. Two-dimensional simulation using $\alpha = 1.35$, $C_1 = 0.1$, and $H = 0.5$. The values of the parameters correspond to what has been evaluated for cloud-radiance pictures in the thermal infrared frequencies range.

Simulations were performed using universal multifractal parameters close to what have been observed for cloud radiances. They are shown in Figs. 33 and 34. Parameters $\alpha = 1.35$, $C_1 = 0.1$ have been used and the value of H is varied because this seemed to be the most important difference between visible and infrared images. For Fig. 33, $H = 0.3$ was used and for Fig. 34 $H = 0.5$ was used. For infrared images, the value of H is higher, giving it the smoother look that meteorologists are familiar with.

7. Conclusions

In the 1950s, before the advent of satellites and high-quality in situ measurement techniques, the mesoscale was postulated to be a dull, inactive energy sink separating dynamically distinct small- and large-scale turbulence. Even from a purely empirical perspective, this standard model now appears to be quite antiquated. In our opinion (which has been voiced regularly since the early 1980s), it is also outdated from a theoretical standpoint: it is predicated on simplistic ideas of isotropic (self-similar) scale invariance. Over the years, the necessity of fully exploring the possible consequences of scale-invariant nonlinear dynamics has led to numerous developments that have enriched our understanding not only of atmospheric dynamics but also of scale invariance itself. We are no longer restricted to studying the geometry of fractal sets; we now have the ability to deal with multifractal statistics and the dynamics of multifractal processes. The existence of universal multifractals—the scaling, nonlinear analogs of the familiar Gaussian variables—makes multifractals increasingly attractive as dynamical models of the atmosphere. Finally, the generalization of scale invariance from a highly restrictive self-similar or self-affine notion to a rich and fruitful symmetry principle provides a challenging new problematic for the geosciences.

In this paper, we have briefly sketched some of these arguments and attempted to succinctly and—as often as possible—graphically present some of the multifractal notions upon which they are based. The object was to motivate the various empirical analyses that followed, as well as to explain the ideas in sufficient detail so that the workings of the new double trace moment (DTM) analysis technique could be grasped. This technique is the first to be designed to directly estimate the universal multifractal parameters; it is considerably more statistically robust than previously existing analysis methods, and it applies not only to "calm" multifractals (the sort associated with strange attractors) but also to the "hard" (extremely variable) multifractals found in geophysics (indeed, we quantitatively confirm the "hard" nature of the cloud radiances and rain reflectivities).

We applied not only the DTM, but also conventional energy spectra to analyze satellite cloud radiances from Landsat, *NOAA-9,* and Meteosat satellites in the visible, near-IR, and thermal IR wavelengths. Overall, the datasets spanned the range 166 m to 4000 km and were found to be scaling through the entire region, including the mesoscale. Although we conclude that the evidence for horizontal scaling is good, it should be stressed that enormous, systematically sampled datasets will be needed to fully characterize the scaling of atmospheric fields as well as the corresponding inner and outer limits. This study only provides an early exploration of what is largely unknown territory.

Moving on from the horizontal scaling of cloud radiances, we analyze data from a vertically pointing radar measuring reflectivities of rain with a resolution of 2.5 s in time, 21 m in space. Here the corresponding scale ratios (the largest divided by the smallest scale) were 2^{13} and 2^{8}, respectively. In time, the scaling was well followed over the range of nearly 20–20 000 s. In the vertical, the scaling was followed at high frequencies, but we found a spectral bump corresponding in size (≈ 1 km) to the thickness of the bright band, which was present throughout the sequence. Since other studies with larger samples (e.g., 20 cases instead of 1) found vertical scaling over the corresponding range, the bump is likely to be consistent with statistical (sample to sample) fluctuations. This conclusion is supported by a space–time DTM analysis that yielded very similar universal multifractal parameters in global daily rainfall accumulations (for 1983). Specifically, the degree of multifractality (characterized by α) was found (within experimental error) to be the same for the in situ gauge measurements and the radar reflectivities. This is perhaps not surprising since α is invariant under the operation of taking powers (such as in the Marshall–Palmer Z–R relation).

Finally, we sketched how our empirically determined multifractal exponents, combined with appropriate space–time transformations, can enable us to make dynamical multifractal simulations. These simulations will be necessary to further our understanding of the underlying atmospheric dynamics. They will help us tame the ubiquitous extreme atmospheric variability, and may have far reaching implications for remote sensing, objective analysis, and (stochastic) forecasting.

Acknowledgments. We thank A. Davis, C. Hooge, P. Hubert, P. Ladoy, D. Lavallée, K. Pflug, F. Schmitt, and B. Watson for helpful comments, discussions, and technical assistance. F. Francis is thanked for helping us in the analysis of the satellites' images, and V. Sahakian and F. Begin are thanked for help with the multifractal simulations. Special thanks to M. Duncan and F. Fabry, who kindly gave us the radar data and improved our understanding of it.

REFERENCES

Atmanspacher, H., H. Scheingraber, and G. Weidenmann, 1989: Determination of $f(\alpha)$ for a limited random point set. *Phys. Rev. A,* **40,** 3954.

Bacry, A., A. Arneodo, U. Frisch, Y. Gagne, and E. Hopfinger, 1989: Wavelet analysis of fully developed turbulence data and measurement of scaling exponents. *Turbulence and Coherent Structures,* M. Lesieur and O. Metais, Eds., Kluwer, 703–718.

Bak, P., C. Tang, and K. Weissenfeld, 1987: Self-organized critical phenomena. *Phys. Rev. Lett.,* **59,** 381–385.

Bellon, A., S. Lovejoy, and G. L. Austin, 1980: A short-term precipitation forecasting procedure using combined radar and satellite data. *Mon. Wea. Rev.,* **108,** 1554–1566.

Beltrami, H., D. Lavallée, C. Hooge, S. Lovejoy, and J. C. Mareschal, 1991: Universal multifractals in earthquakes. *Eos,* **72,** 279.

Benzi, R., G. Paladin, G. Parisi, and A. Vulpiani, 1984: On the multifractal nature of fully developped turbulence and chaotic system. *J. Phys.,* **A17,** 3521–3531.

Brax, P., and Pechanski, R., 1991: Levy stable law description on intermittent behaviour and quark-gluon phase transitions. *Phys. Lett. B,* 225–230.

Brenier, P., 1990: Simulations dynamique multifractale des nuages. M.S. thesis. Ecole Normale de Science et Technologie, Paris, France,

——, D. Schertzer, G. Sarma, J. Wilson, and S. Lovejoy, 1990: Continuous multiplicative cascade models of passive scalar clouds. *Ann. Geophys.,* **8** (Special Issue), 320.

Carter, B., and R. N. Henrickson, 1991: A systematic approach to self-similarity in Newtonian space/time. *J. Math. Phys.,* **32**(10), 2580–2597.

Chhabra, A. B., and K. R. Sreenivasa, 1991: Negative dimensions: Theory, computation and experiments. *Phys. Rev. A,* **34,** 1114.

Corrsin, S., 1951: On the spectrum of isotropic temperature fluctuations in an isotropic turbulence. *J. Appl. Phys.,* **22,** 469–473.

Davis, A., S. Lovejoy, and D. Schertzer, 1991: Radiative transfer in multifractal media. *SPIE Proc.,* **1558,** 37–59.

Fan, A. H., 1989: Chaos additif et multiplicatif de Levy. *C. Rcy. Acad. Sci. Paris,* **1**(308), 151–154.

Frisch, U. P., P. L. Sulem, and M. Nelkin, 1978: A simple dynamical model of intermittency in fully develod turbulence. *J. Fluid Mech.,* **87,** 719–724.

Gabriel, P., S. Lovejoy, D. Schertzer, and G. Austin, 1988: Multifractal analysis of resolution dependence in satellite imagery. *Geophys. Res. Lett.,* **15,** 1373–1376.

Gage, K. S., 1979: Evidence for a $k^{-5/3}$ law inertial range in mesoscale two-dimensional turbulence. *J. Atmos. Sci.*, **36**, 1950.

Grassberger, 1983: Generalized dimensions of strange attractors. *Phys. Rev. Lett.*, **A97**, 227.

Gupta, V. K., and E. Waymire, 1990: Multiscaling properties of spatial rainfall and river flow distributions. *J. Geophys. Res.*, **95**, 1999–2010.

——, and ——, 1991: On lognormality and scaling in spatial rainfall averages? *Nonlinear Variability in Geophysics, Scaling and Fractals*, D. Schertzer and S. Lovejoy, Eds., 175–184.

Halsey, T. C., M. H. Jensen, L. P. Kadanoff, I. Procaccia, and B. Shraiman, 1986: Fractal measures and their singularities: The characterization of strange sets. *Phys. Rev. A*, **33**, 1141–1151.

Hentschel, H. G. E., and I. Proccacia, 1983: The infinite number of generalized dimensions of fractals and strange attractors. *Physica*, **8D**, 435–444.

Hubert, P., Y. Tessier, P. Ladoy, S. Lovejoy, D. Schertzer, J. P. Carbonnel, S. Violette, I. Desurosne, and F. Schmitt, 1992: Multifractals and extreme rainfall events. *Geophys. Res. Lett.*, in press.

Keddem, B., and L. S. Chiu, 1987: Are rain rate processes self-similar? *Wat. Resour. Res.*, **23**, 1816–1818.

Kolmogorov, A. N., 1940: Wienersche spiralen and einige andere interessante kurven in Hilbertschen Raum. *C. R. (Doklady) Acad. Sci. URSS (N.S.)*, **26**, 115–118.

——, 1941: Local structure of turbulence in an incompressible liquid for very large Reynolds numbers. *Proc. Acad. Sci. USSR., Geochem. Sect.*, **30**, 299–303.

——, 1962: A refinement of previous hypotheses concerning the local structure of turbulence in viscous incompressible fluid at high Reynolds number. *J. Fluid Mech.*, **83**, 349.

Ladoy, P., S. Lovejoy, and D. Schertzer, 1991. Extreme Variability of climatological data: Scaling and intermittency. *Scaling, Fractals and Non-Linear Variability in Geophysics*, D. Schertzer and S. Lovejoy, Eds. Kluwer.

——, F. Schmitt, D. Schertzer, and S. Lovejoy, 1992: Analyse Multifractale de la variabilité temporelle des observations pluviométriques a Nimes. *C. Roy. Acad. Science*, submitted.

Lamperti, J., 1962: Semi-stable stochastic processes. *Trans. Amer. Math. Soc.*, **104**, 62–78.

Lavallée, D., 1991: Multifractal techniques: Analysis and simulation of turbulent fields. Ph.D. thesis, McGill University, Montréal, Canada.

——, D. Schertzer, and S. Lovejoy, 1991a: On the determination of the codimension function. *Scaling, Fractals and Non-Linear Variability in Geophysics.* D. Schertzer and S. Lovejoy, Eds., Kluwer.

——, S. Lovejoy, D. Schertzer, and P. Ladoy, 1991b: Nonlinear variability and Landscape topography: Analysis and simulation. *Fractals in Geography*, L. De Cola and N. Lam, Eds.

Lilly, D. K., 1983: Meso-scale variability of the atmosphere. *Mesoscale Meteorology—Theories, Observations and Models*, D. K. Lilly and T. Gal-Chen, Eds., D. Reidel, 13–24.

Lovejoy, S., 1981: Analysis of rain areas in terms of fractals. *Proc. 20th Conf. on Radar Meteorology*, Amer. Meteor. Soc., 476–484.

——, 1982: Area-perimeter relations for rain and cloud areas. *Science*, **187**, 1035–1037.

——, and B. Mandelbrot, 1985: Fractal properties of rain and a fractal model. *Tellus*, **37A**, 209.

——, and D. Schertzer, 1985: Generalised scale invariance and fractal models of rain. *Wat. Resour. Res.*, **21**, 1233–1250.

——, and ——, 1986: Scale invariance, symmetries, fractals, and stochastic simulations of atmospheric phenomena. *Bull. Amer. Meteor. Soc.*, **67**, 21–32.

——, and ——, 1989: Comments on "Are rain rate proceses self-similar?" *Wat. Resour. Res.*, **25**, 577–579.

——, and ——, 1990a: Our multifractal atmosphere: A unique laboratory for non-linear dynamics. *Can. J. Phys.*, **46**, 62.

——, and ——, 1990b: Multifractals, universality classes and satellite and radar measurements of clouds and rain fields. *J. Geophys. Res.*, **95**, 2021.

——, and ——, 1990c: Fractals, rain drops and resolution dependence of rain measurements. *J. Appl. Meteor.*, **29**, 1167–1170.

——, and ——, 1991: Multifractal analysis techniques and the rain and clouds fields from 10^{-1} to 10^{6} m. *Scaling, Fractals and Non-Linear Variability in Geophysics*, D. Schertzer and S. Lovejoy, Eds. Kluwer, 111–144.

——, ——, and P. Ladoy, 1986: Fractal characterisation of inhomogeneous measuring networks. *Nature*, **319**, 43–44.

——, ——, and ——, 1987a: Brighter outlook for weather forecasts. *Nature*, **320**, 401.

——, ——, and A. A. Tsonis, 1987: Functional box-counting and multiple elliptical dimensions in rain. *Science*, **235**, 1036–1038.

——, ——, and K. Pflug, 1992: Generalized scale invariance and differential rotation in cloud radiances. *Physica A*, **185**, 121–128.

——, ——, P. Silas, Y. Tessier, and D. Lavallée, 1992: The unified scaling model of atmospheric dynamics and systematic analysis in cloud radiances. *Ann. Geophys.*, in press.

Mandelbrot, B., 1974: Intermittent turbulence in self-similar cascades: Divergence of high moments and dimension of the carrier. *J. Fluid Mech.*, **62**, 331–350.

——, and J. W. Van Ness, 1968: Fractional Brownian motions, fractional noises and applications. *SIAM Rev.*, **10**, 422–450.

Meneveau, C., and K. R. Sreenivasan, 1987: Simple multifractal cascade model for fully developed turbulence. *Phys. Rev. Lett.*, **59**(13), 1424–1427.

——, and ——, 1989: Measurement of $f(\alpha)$ from scaling of histograms, and applications to dynamical systems and fully developped turbulence. *Phys. Lett. A*, **137**, 103–112.

Monin, A. S., 1972: *Weather Forecasting as a Problem in Physics.* MIT Press.

Nastrom, G. D., and K. S. Gage, 1983: A first look at wave-number spectra from GASP data. *Tellus*, **35**, 383.

Novikov, E. A., and R. Stewart, 1964: Intermittency of turbulence and spectrum of fluctuations in energy-dissipation. *Izv. Akad. Nauk. SSSR. Ser. Geofiz.*, **3**, 408–412.

Obhukhov, A., 1949: Structure of the temperature field in a turbulent flow. *Izv. Akad. Nauk. SSSR Ser. Geogr. I Jeofiz*, **13**, 55–69.

——, 1962: Some specific features of atmospheric turbulence. *J. Geophys. Res.*, **67**, 3011.

Paladin, G., and A. Vulpiani, 1987: Anomalous scaling laws in multifractal objects. *Phys. Reports*, **156**, 147–225.

Parisi, G., and U. Frish, 1985: A multifractal model of intermittency. *Turbulence and Predictability in Geophysical Fluid Dynamics and Climate Dynamics*, M. Ghil, R. Benzi, and G. Parisi, Eds. North-Holland, 84–88.

Pflug, K., S. Lovejoy, and S. Schertzer, 1991: Generalized scale invariance, differential rotation and cloud texture. *Nonlinear Dynamics of Structures*, R. Z. Sagdeev, U. Frish, A. S. Moiseev, and A. Erokhim, Eds. World Scientific, 72–78.

——, ——, and ——, 1993: Generalized scale invariance, differential rotation and cloud texture. *J. Atmos. Sci.*, **50**, in press.

Richardson, L. F., 1922: *Weather Prediction by Numerical Process.* Cambridge University Press

Schertzer, D., and S. Lovejoy, 1983: Elliptical turbulence in the atmosphere. *Proc. 4th Symp. on Turbulent Shear Flows*, Karlshule, West Germany, 11.1–11.8.

——, and ——, 1985a: The dimension and intermittency of atmospheric dynamics. *Turbulent Shear Flow 4*, B. Launder, Ed., Springer-Verlag, 7–33.

——, and ——, 1985b: Generalised scale invariance in turbulent phenomena. *Phys. Chem. Hydrodyn. J.*, **6**, 623–635.

——, and ——, 1987a: Singularités anisotropes, divergence des moments en turbulence: Invariance d'échelle généralisée et processus multiplicatifs. *Ann. Sci. Math. du Québec*, **11**(1), 139–181.

——, and ——, 1987b: Physical modeling and analysis of rain and clouds by anysotropic scaling of multiplicative processes. *J. Geophys. Res. D*, **92**(8), 9693–9714.

——, and ——, 1989a: Nonlinear variability in geophysics: Multifractal analysis and simulation. *Fractals: Physical Origin and Consequences,* L. Pietronero, Ed., Plenum, 49.

——, and ——, 1989b: Generalized scale invariance and multiplicative processes in the atmosphere. *Pageoph,* **130,** 57–81.

——, and ——, 1991: Nonlinear geodynamical variability: Multiple singularities, universality and observables. *Scaling, Fractals and Non-Linear Variability in Geophysics,* D. Schertzer and S. Lovejoy, Eds. Kluwer, 41–80.

——, and ——, 1992: Hard and soft multifractal processes. *Physica A,* **185,** 187–194.

——, ——, R. Visvanthan, D. Lavallée, and J. Wilson, 1988: Multifractal analysis techniques and rain and cloud fields. *Fractal Aspects of Materials: Disordered Systems,* D. A. Weitz, L. M. Sander, and B. B. Mandelbrot, Eds. Materials Research Society, 267–270.

——, ——, D. Lavallée, and F. Schmitt, 1991: Universal hard multifractal turbulence: Theory and observation. *Nonlinear Dynamics of Structures,* R. Z. Sagdeev, U. Frish, A. S. Moiseev, and A. Erokhin, Eds. Holland, 213–235.

——, ——, and D. Lavallée, 1992: Genmeric first order phase transitions in multifractal processes. *Phys. Rev. Lett.*, submitted.

Schmitt, F., S. Lovejoy, D. Schertzer, D. Lavallée, and C. Hooge, 1992a: First estimates of multifractal indices for velocity and temperature fields. *C. R. Acad. Sci. de Paris.*

——, D. Lavallée, D. Schertzer, and S. Lovejoy, 1992b: Empirical determination of universal multifractal exponents in turbulent velocity fields. *Phys. Rev. Lett.,* **68,** 305–308.

——, D. Schertzer, S. Lovejoy, and D. Lavallée, 1992c: Universal multifractal indices and order of divergence of moments for atmospheric turbulent wind data. *Phys. Fluids,* submitted.

Seed, A., 1989: Statistical problems in measuring convective rainfall. PhD. thesis, McGill University, 141 pp.

Taylor, G. I., 1938: The spectrum of turbulence. *Proc. Roy. Soc.,* **A164**(919), 476–490.

Tessier, Y., D. Lavallée, S. Lovejoy, and D. Schertzer, 1992a: Multifractal indices of the ocean surface: Deduced by the double trace moment technique. *Geophys. Res. Lett.*, submitted.

——, S. Lovejoy, and D. Schertzer, 1992b: Multifractal objective analysis and global rainfall. *J. Geophys. Res.*

Vinnichencko, N. K., 1969: The kinetic energy spectrum in the free atmosphere for 1 second to 5 years. *Tellus,* **22,** 158–165.

Waymire, E., 1985: Scaling limits and self-similarity in precipitation fields. *Wat. Resour. Res.,* **21,** 1271–1281.

Wilson, J., D. Schertzer, and S. Lovejoy, 1991: Physically based cloud modelling by multiplicative cascade processes. *Scaling, Fractals and Non-Linear Variability in Geophysics,* D. Schertzer and S. Lovejoy, Eds., 185–207.

Yaglom, A. M., 1966: The influence of the fluctuation in energy dissipation on the shape of turbulent characteristics in the inertial interval. *Sov. Phys. Dokl.,* **2,** 26–30.

Zawadzki, I., 1973: Statistical properties of precipitation patterns. *J. Appl. Meteor.,* **12,** 469–472.